Nanoscale

REVIEW

View Article Online
View Journal | View Issue

Cite this: *Nanoscale*, 2026, **18**, 7882

Catalytic tango in diatomic catalysts: from precision-guided pair construction to machine-learning-driven identification and design

Bowen Jiang, [a] Jishui Huang, [b] Kuibo Yin *[a] and Litao Sun *[a]

Diatomic catalysts (DACs) are composed of two neighboring metal centers, each stabilized by its own coordination environment, that extend single-atom precision into a cooperative two-site manifold. By programmably tuning composition, geometry, and local microenvironment, DACs bridge the gap between isolated single-atom sites and extended clusters, and can enable cross-site electronic coupling, dual-site adsorption motifs, and short-range relay pathways that are difficult to realize on mononuclear sites, effectively creating a catalytic "tango" in which two adjacent centers cooperate through shared electronic structure and intermediates. This Review first highlights strategies for precision-guided pair construction, including probability-controlled density generators that increase the likelihood of forming adjacent sites, ordered coordination networks (MOFs, COFs, and related 2D frameworks) that pre-organize metal nodes at defined separations, and multinuclear metal–organic complexes that offer molecular blueprints for well-defined dimers and higher oligomers. These platforms are then used to discuss representative modes of intersite cooperativity: charge redistribution and orbital hybridization between neighboring metals, distance- and orientation-dependent co-adsorption and transition states on dual sites, and sequential reaction pathways in which different elementary steps are preferentially accommodated by different atoms in the pair. Finally, the Review surveys how atomic-resolution electron microscopy and related correlative imaging are beginning to be combined with machine-learning workflows for automatic identification, classification, and screening of neighboring metal sites, sketching an emerging and promising route toward machine-learning-assisted identification and design of diatomic motifs.

Received 5th December 2025,
Accepted 5th March 2026

DOI: 10.1039/d5nr05121e

rsc.li/nanoscale

1. Introduction

1.1 Motivation and definition of DACs

The evolution from nanoparticle to single-atom catalysts (SACs) represents a paradigm shift in heterogeneous catalysis, achieving near-atomic metal utilization and site precision.[1–3] This pursuit of atomic-scale site engineering resonates conceptually with biocatalysis, where the precise configuration of metal cofactors is central: a survey of 130 033 enzyme entries in the RCSB PDB (snapshot dated Oct 24, 2025) indicates that more than 54 337 enzymes feature trace metal cofactors such as Fe, Zn, and Cu that drive essential metabolic processes with remarkable efficiency.[4,5] However, the isolation intrinsic to SACs, while maximizing metal exposure, imposes constraints akin to a solo performance: the inherent single-site bottleneck forces incompatible adsorption and activation requirements onto a lone center, constraining multistep chemistry and leading to activity loss and structural instability during operation.[6–8]

Intriguingly, nature has elegantly addressed similar catalytic challenges through multi-metal cooperation. Analysis of metalloenzymes reveals that 74.2% (40 330 characterized enzymes) feature active sites incorporating two or more metal atoms.[9] This prevalence of multi-metal motifs underscores a fundamental biological strategy: leveraging synergistic interplay between adjacent metal centers to achieve catalytic feats unattainable by isolated atoms. A prime example is the Mn_4CaO_5 cluster in Photosystem II (PSII),[10] which links four Mn and one Ca atom *via* five μ-oxo bridges. This unique multi-metal center orchestrates the demanding, room-temperature water splitting into oxygen, protons, and electrons. In the same spirit, soluble methane monooxygenase uses a carboxylate-bridged di-iron center to activate O_2 and oxidize methane under ambient conditions,[11] while [NiFe] hydrogenases rely on a compact Ni–Fe core for rapid, reversible H_2 activation with exquisite redox tuning.[12,13] Motivated by these lessons, catalyst design is shifting beyond SACs toward architectures that preserve atomic precision while enabling multi-site

[a]*SEU-FEI Nano-Pico Center, Key Lab of MEMS of Ministry of Education, Southeast University, Nanjing 210096, P. R. China. E-mail: yinkuibo@seu.edu.cn, slt@seu.edu.cn*
[b]*College of Aerospace Engineering, Nanjing University of Aeronautics and Astronautics, Nanjing 210016, P. R. China*

cooperation.[14–16] The term diatomic catalysts (DACs) denotes catalytic architectures composed of two neighboring, atomically dispersed metal centers anchored on a support. Each center is stabilized by its own coordination environment, with the two centers separated by a tunable Å-scale intersite distance ($d_{M–M}$),[17,18] and the metal combination may be homo or heteronuclear. The pair remains non-aggregated and distinct from clusters or nanoparticles, yet close enough to permit cross-site electronic communication, bridged adsorption, and tandem reaction steps.[15,16]

By rationally tuning the $d_{M–M}$, nuclearity and composition, and local coordination environment, DACs can relieve the single-site limitations of SACs and unlock dual-site reaction channels that are difficult to access on isolated atoms. A number of valuable reviews have already highlighted key facets of this emerging field, including MOF- and COF-derived frameworks for controllable anchoring and derivation,[19,20] design principles and applications of heteronuclear pairs,[21] intermetal electronic interactions as the mechanistic basis for activity and selectivity,[14] $d_{M–M}$ as a geometry-governed activity descriptor in electrocatalysis,[22] and reaction-specific microenvironment or active-moiety regulation with explicit structure–performance correlations across electrocatalysis.[23]

1.2 Current challenges

Despite rapid progress, research on DACs still lacks a coherent structure–function framework.[19,24] In particular, the relationships between pair construction, adjacency-induced effects, and *operando* structural identification remain insufficiently established, complicating reaction-specific DACs selection.[25–27] The synthesis–structure map is often route-dependent and not easily mechanistically disentangled, while current characterization methods rarely resolve geometric structure, electronic configuration, and *operando* state within a unified evidence chain.[17,28] These limitations hinder the transferability of design principles and highlight the need for more rigorous, quantitatively reliable metrology and screening strategies.

First, pair construction is partially controllable in terms of intersite distance and metal identity. Many synthetic approaches generate broad distance distributions,[17] and achieving high pair purity, particularly for heteronuclear pairs with defined sequence and local symmetry, competes with diffusion, reconstruction, and sintering processes.[29,30] As a result, isolated atoms, genuine diatomic pairs, and small clusters often coexist within the same support.[31] Although these motifs may exhibit similar averaged coordination signatures,

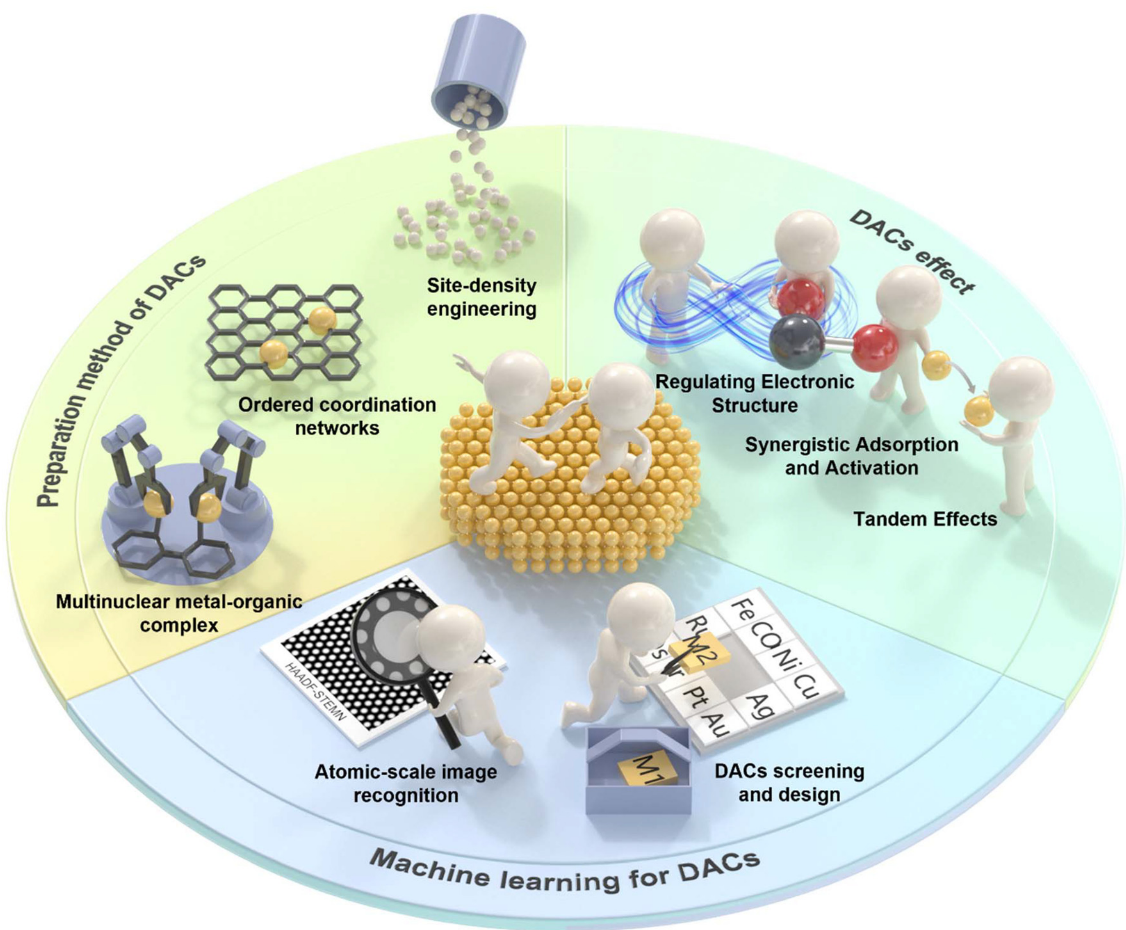

Fig. 1 Build–Effect–Identify & Screen: a single-figure overview of DACs.

their catalytic behaviors can differ substantially. Such structural heterogeneity complicates reproducibility and poses additional challenges for scalable and precision-controlled synthesis.[19]

Second, site identification remains a critical bottleneck. The presence of two bright spots in a High-Angle Annular Dark-Field Scanning Transmission Electron Microscopy (HAADF-STEM) image does not necessarily confirm a well-defined diatomic active site, and ensemble-averaged techniques may obscure the distinction between isolated atoms, true pairs, and small clusters when they coexist. Under reaction conditions, coordination environment, oxidation state, and site populations can dynamically evolve, making the active-site definition condition-dependent.[27] Reliable site assignment requires correlative approaches that integrate local microscopy, *operando* spectroscopy, and statistically meaningful sampling to quantify site populations, rather than relying solely on representative images.[32]

Third, linking catalytic performance to a specific DACs structure under operating conditions remains challenging. The two metal centers may interchange between terminal and bridging adsorption modes, while their oxidation and coordination states can shift with applied potential, electrolyte environment, and surface coverage.[25–27] Because the population of each adsorption state is dynamic, activity and selectivity trends may not correlate directly with static *ex situ* descriptors.[30] This often necessitates empirical optimization across composition, intersite distance, coordination environment, and operating conditions.[24]

1.3 Scope of the review

To address these needs, we organize this review into three modules (Fig. 1). Build benchmarks construction routes and their controllability, together with inherent uncertainties. Effect summarizes transferable cooperative mechanisms enabled by adjacency. Identify & Screen highlights metrology and machine-learning-enabled workflows that translate atomic-scale information into auditable metrics and actionable design rules.

2. Preparation methods of DACs

This Review organizes DACs synthesis strategies according to the degree of structural control they offer. In terms of structural control, the methods range from statistical approaches to reticular frameworks and finally to nearly deterministic strategies. First, site-density engineering (section 2.1) increases the probability of forming neighboring pairs by tuning metal/anchor density and deposition sequence; they narrow the distribution of intersite distances without enforcing a single geometry, which is attractive when throughput and scalability dominate. Second, ordered coordination networks (section 2.2)—including MOFs, COFs/2D polymers, and other ordered inorganic scaffolds—impose Å-scale spacing and symmetry at the node, linker, or pore level and can transfer this registry through constrained conversion or low-temperature fixation, providing reticular control with small variance across many sites. Third, multinuclear metal–organic complexes (MOCs, section 2.3) supply molecular blueprints with predefined d_{M-M}, ligand fields, and bridging patterns; when immobilized and stepwise de-ligated under low-mobility conditions, they yield homo- or heteronuclear pairs with the highest uniformity. These classes are not mutually exclusive: hybrid or sequential routes—such as site-density engineering-enriched anchors within an ordered network, MOCs that set heteronuclear identity, or combinations with ALD-style temporal control—can further tighten d_{M-M} distributions, reduce site-geometry dispersion, and improve pair purity beyond what any single method can achieve.

2.1 Site-density engineering (density & time series)

The site-density engineering increases the surface density of metal atoms and neighboring anchoring sites and programs deposition flux and sequence, thereby statistically raising the probability of adjacent occupancy and biasing the ensemble toward paired configurations, including multi-atom arrangements.[28,33] This probability-driven route has become a mainstream practice in recent years: by elevating metal loading or the number of anchoring sites,[18,22,34] following the simple logic that higher loading narrows intersite separations, one can, without changing the overall processing framework, achieve coarse-grained formation of diatomic motifs and related near-neighbor states.

Building on this logic, site-density engineering can be operationalized through three practical levers that often act additively on encounter probability: first, raise the areal density of metal precursors by increasing nominal loading, using co impregnation with multiple metals, or supplying a vapor phase feed to saturate accessible anchors;[34,35] second, increase the areal density and local multiplicity of occupiable, closely spaced anchoring sites through defect engineering, N/O/S/P heteroatom doping, surface functionalization, acid or base etching to create vacancies, or plasma activation, thereby generating more coordination pockets or defect pairs per unit area at shorter separations;[36–38] third, program the time domain of deposition by tuning flux, pulse width, and sequence so nascent adatoms encounter one another before they are trapped by long range diffusion or converted to species with lower mobility.[28,33]

2.1.1 Raising the areal density of metal precursors. The first lever increases the likelihood of joint occupancy simply by narrowing average intersite separations at higher nominal loading. A canonical example is the study of neighboring Pd single atoms on an inert support, where isolated (i-Pd_1) and neighboring (n-Pd_1) sites were distinguished and a clear, loading-dependent shift toward n-Pd_1 was observed—clean evidence that higher metal density statistically boosts the neighbor fraction without invoking particle growth.[31]

This loading–spacing connection has been further quantified in recent work: by systematically tuning surface loading, Zhang and co-workers[39] mapped how the accessible site density and effective intersite separations evolve with coverage, identifying an intermediate loading window that maximizes kinetic readouts (overpotential, Tafel slope, charge-transfer resistance), consistent with a cooperative regime rather than the dilute, non-interacting limit. In parallel, Yu and co-workers[17] directly resolved the role of the d_{M-M} in Fe–N_4–C for oxygen reduction reaction (ORR, Fig. 2a): when d_{M-M} converges into a sub-nanometer to about 1.2 nm window, both mass activity and intrinsic activity rise markedly, whereas overly short spacing risks adverse overlap and performance roll-off. Together, these datasets articulate the site-density engineering mechanism in practice: raising loading increases the statistical odds of near-neighbor occupancy, and there exists a finite spacing window where pairwise electronic coupling delivers the strongest catalytic benefit.

2.1.2 Neighboring anchoring-site density. On carbide and reducible-oxide supports, researchers now deliberately write in adjacent traps and meter metal flux to bias single atoms toward neighboring occupancy—without predefining molecular geometry. Zhang *et al.*[40] first produced defect-rich Mo_2C by controlled carburization (CH_4/H_2 or C_2H_2/H_2; tuned temperature/ramp), then introduced Pt by ultradilute incipient-wetness dosing of H_2PtCl_6 or organoplatinum, followed by low-temperature H_2 activation and multi-aliquot micro-dosing; under these conditions Pt preferentially arrests at paired surface defects, yielding quasi-paired Pt single atoms (Fig. 2b, second-shell contact, no aggregation). Translating the same lever to reducible oxides, Lou *et al.*[41] pre-generated adjacent oxygen-vacancy couples on CeO_2 by H_2/Ar or chemical reduction, then deposited sub-monolayer Pd either as binuclear precursors or as equimolar salts *via* capillary impregnation, followed by gentle drying and reduction to lock Pd dimers across the vacancy pairs, forming Pd_2O_4-type local motifs and suppressing long-range migration. Likewise, Shi *et al.*[42] prepared oxygen-vacancy–rich TiO_{2-x} nanosheets by $NaBH_4$ or H_2 reduction, with optional plasma treatment, creating dense traps composed of oxygen vacancies and Ti(III) centers. They then introduced dilute H_2PtCl_6 and $RuCl_3$ either together or in sequence, so the second metal preferentially occupied the vacancy adjacent to the site seeded by the first; gentle annealing or photochemical reduction fixed neighboring Pt–Ru atomic centers and removed weakly bound ligands.

On the carbon side, several groups have explicitly densified and brought neighboring N-anchors into closer proximity to bias metals toward near-neighbor configurations. Deng *et al.*[43] mixed cobalt/nickel acetates with L-alanine and melamine,

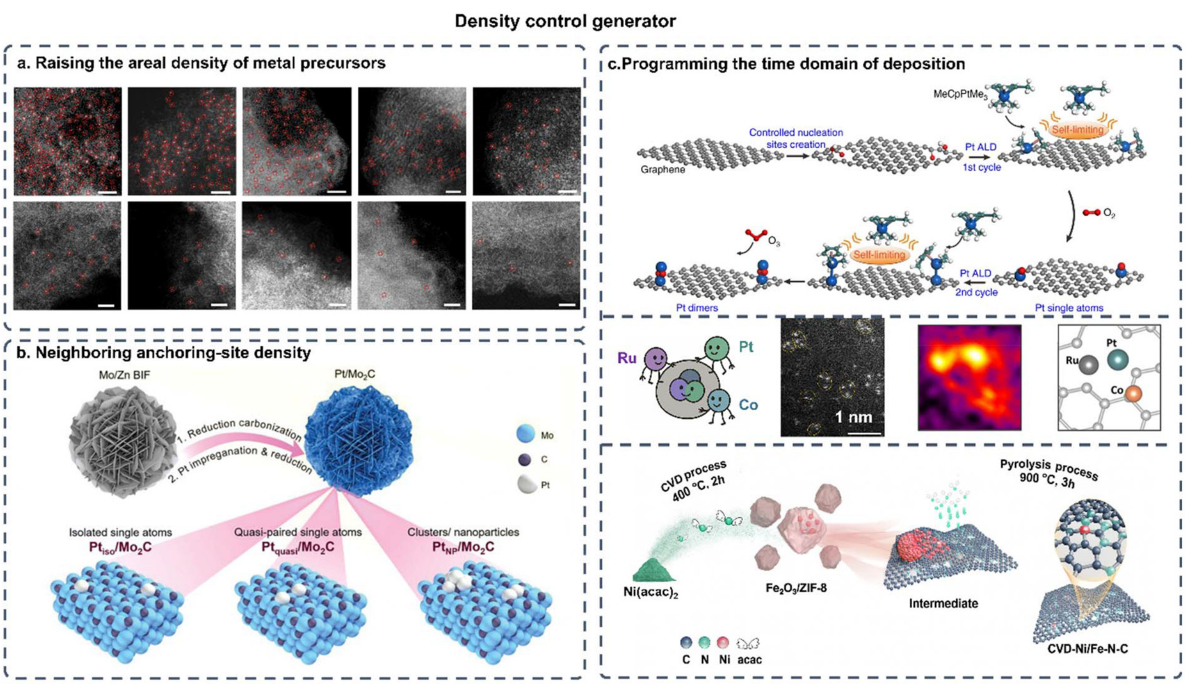

Fig. 2 (a) HAADF-STEM images of Fe–N_4–C catalysts with systematically tuned d_{M-M} (0.5, 0.7, 0.9, 1.2, 1.9, 2.6, 3.2, 4.6, 5.2, and 7.8 nm) by varying metal loading. Adapted from ref. 17 with permission from Springer Nature, copyright 2021. (b) Schematic diagram of the materials synthesis of quasi-paired Pt single atoms. Adapted from ref. 40 under the Creative Commons CC-BY license. (c) Top: schematic of the bottom-up fabrication of dimeric Pt_2 sites on graphene. First, isolated anchor sites are created on pristine graphene. Second, one Pt-ALD cycle (alternating $MeCpPtMe_3$ and O_2 pulses) populates these anchors with Pt_1 atoms. Third, a second, lower-temperature Pt-ALD cycle selectively places a second Pt atom onto the pre-existing Pt_1 to yield Pt_2 dimers. (Pt, blue; O, red; H, white; C in surface groups, cyan; C in the graphene lattice, gray.) Adapted from ref. 44 under the Creative Commons CC-BY license. Middle: schematic of an asymmetric Pt–Ru–Co triple-atom catalyst (TACs), HAADF-STEM images highlighting Pt–Ru–Co TACs (yellow dotted circles), and local electron-intensity line profile across a representative Pt–Ru–Co TACs; and the corresponding structural model. Adapted from ref. 28 and 45 with permission from Elsevier, copyright 2025. Bottom: schematic of the CVD process to prepare high-density atomic dispersed Ni/Fe DACs. Adapted from ref. 46 under the Creative Commons CC-BY license.

carried out a two-step pyrolysis, followed by HCl leaching and a second anneal, thereby generating N-doped graphene rich in closely spaced coordination mouths and stabilizing Co/Ni diatomic sites within that environment. Wang *et al.*[29] devised an atmosphere-programmable carbonization strategy to toggle Fe between single sites and pairs. They obtained Fe_1–N_4–C. Using 5% H_2/Ar shifted the product to *ortho*-coupled Fe_2–N_6–C. At 10% H_2/Ar it transformed to *para*-coupled Fe_2–N_6–C. At higher hydrogen levels around 20% it favored Fe_1–N_3–C. Increasing hydrogen converts pyridinic and pyrrolic N to graphitic N and introduces additional porosity and defects, which changes the types and spacing of N anchoring pockets and biases Fe placement. A short, low-migration post-treatment then fixes the targeted configuration, providing a concise and controllable route to carbon-supported Fe_2–N_6–C.

2.1.3 Programming the time domain of deposition. Diatomic-site construction can be cast as a timing problem: deliberately opening a finite encounter window so freshly created adatoms can make a few short hops and find a neighbor before long-range diffusion or deep fixation. In Atomic layer deposition (ALD) style sequential pulses, the window is encoded directly in pulse order and width.

Yan *et al.*[44] established a bottom-up ALD scheme. They first seeded isolated Pt atoms on phenolic anchor sites of graphene by alternating $MeCpPtMe_3$ and O_2. A second, lower-temperature Pt cycle with O_3 then placed a second Pt selectively on pre-existing Pt_1, forming Pt_2 dimers. This seed–activation–second-feed cadence narrows the mobility window and suppresses aggregation, as shown in Fig. 2c top. Sun *et al.*[28,45] applied order-controlled sequential ALD on N-doped carbon nanotubes, Pt followed by Ru and then Co, and showed that preserving this sequence is essential for building stable multi-atom motifs, whereas changing the order leads to clustering. A representative higher-order outcome, the asymmetric Pt–Ru–Co triple-atom motif and its experimental/structural readouts, is illustrated in Fig. 2c middle. Qi *et al.*[46] devised a metal–organic chemical vapor deposition (CVD) protocol that preset Fe–N–C and then introduced a volatile Ni precursor with purge/flash steps. Keeping the Fe-first, Ni-later sequence enabled atomic-level Ni infiltration into Fe_2O_3@ZIF-8-derived frameworks, enriching neighboring Fe–Ni sites while maintaining dispersion (Fig. 2c bottom).

These approaches regulate pulse width, exposure time, and temperature to control atomic mobility and pairing probability. By limiting uncontrolled migration, they improve reproducibility and sequence control within standard ALD or CVD systems.

2.2 Ordered coordination networks for DACs (Pre-writing & Inheritance)

Ordered coordination networks are crystalline or quasi-crystalline framework/interfacial systems that exhibit atomic-scale periodicity and site programmability, allowing the lattice to predefine the geometric and electronic environment of metal anchoring sites. This class includes MOFs, COFs and two-dimensional coordination polymers, and ordered inorganic substrates with lattice-defined terraces or pore/defect arrays (oxides, zeolites, carbides and nitrides). These networks convert chance adjacency into a programmable structural variable for DACs. By encoding $d_{M\text{–}M}$, donor identity, and the local electrostatic field directly into crystalline lattices, these hosts preorganize two single-metal centers and then transfer this registry *via* mild coordination editing or controlled conversion into robust, catalytically competent environments. The result is not just two atoms close in space, but two atoms embedded in a deliberately engineered microenvironment that promotes cooperative adsorption, charge redistribution, and multi-center elementary steps.

2.2.1 MOFs—reticular encoding and inheritable adjacency. MOFs enable reticular, rule-based encoding of adjacency across the framework—at the levels of nodes, linkers, and pores—and preserve it during conversion. Lattice periodicity prespecifies metal separation and orientation, while coordination fields and channel confinement limit diffusion and redox mobility during activation, so sub-nanometer, non-metal–metal-bonded proximity is retained with high fidelity. Thus, pairing shifts from chance encounters to pre-programmed geometry, turning reticular blueprints into inheritable adjacency in the final catalyst.

2.2.1.1 Node level. In the node-blueprint inheritance route, frameworks bearing volatile/replaceable nodes first write the desired anchor density and relative placement into the lattice. Subsequent carbonization/carbonitridation then transfers this node blueprint into a conductive host, after which sequential impregnation/activation fixes two metals within node-proximal pockets. For example, Xiao *et al.*[47] programmed nearest-neighbor statistics in bimetallic Zn, Co-ZIFs, and under a low-mobility conversion window, inherited that registry into N–C to form binuclear Co_2N_5 sites with order-of-magnitude higher per-site ORR activity than CoN_4. Li *et al.*,[48] who started from Cu_3(benzene-1,3,5-tricarboxylate)$_2$, co-mixed an N source, carried out inert pyrolysis, and acid-etched nanoparticles to anchor Cu–Cu and Cu–Ni neighbors on N-doped carbon. Next, Cheng *et al.*[49] used a MOFs-derived N-doped carbon, loading Ni first and then Cu, followed by a second activation to construct Ni–Cu neighbors. Later, He *et al.*[50] co-introduced Fe/Co into ZIF-8 and, after programmed carbonization and mild acid leaching, obtained Fe–Co neighboring pairs. Most recently, Ren *et al.*[51] reported a blueprint-based ion-exchange/two-solvent variant: beginning with Fe-doped ZIF-8 (Fe bound at the node), they added methanolic $Ni(NO_3)_2$ dropwise into an n-hexane dispersion of the Fe-ZIF-8 to encapsulate Ni in sub-5 Å cavities, then performed high-temperature pyrolysis to volatilize Zn nodes, yielding isolated diatomic Ni–Fe M–N_x sites on N-doped carbon for CO_2 Reduction Reaction (CO_2RR). Additionally, Shu *et al.*[52] showed in the heterobimetallic MOFs MUV-102(Cu–Ti) (Fig. 3a) that node-level metal programming (controlling Cu/Ti occupancy and arrangement) can tune Lewis acidity and generate abundant open metal sites, thereby enabling high-capacity, cyclable NH_3 uptake. This finding indicates that node metal composition and architecture are potent upstream design levers, fully compatible with blueprint inheritance prior to conversion.

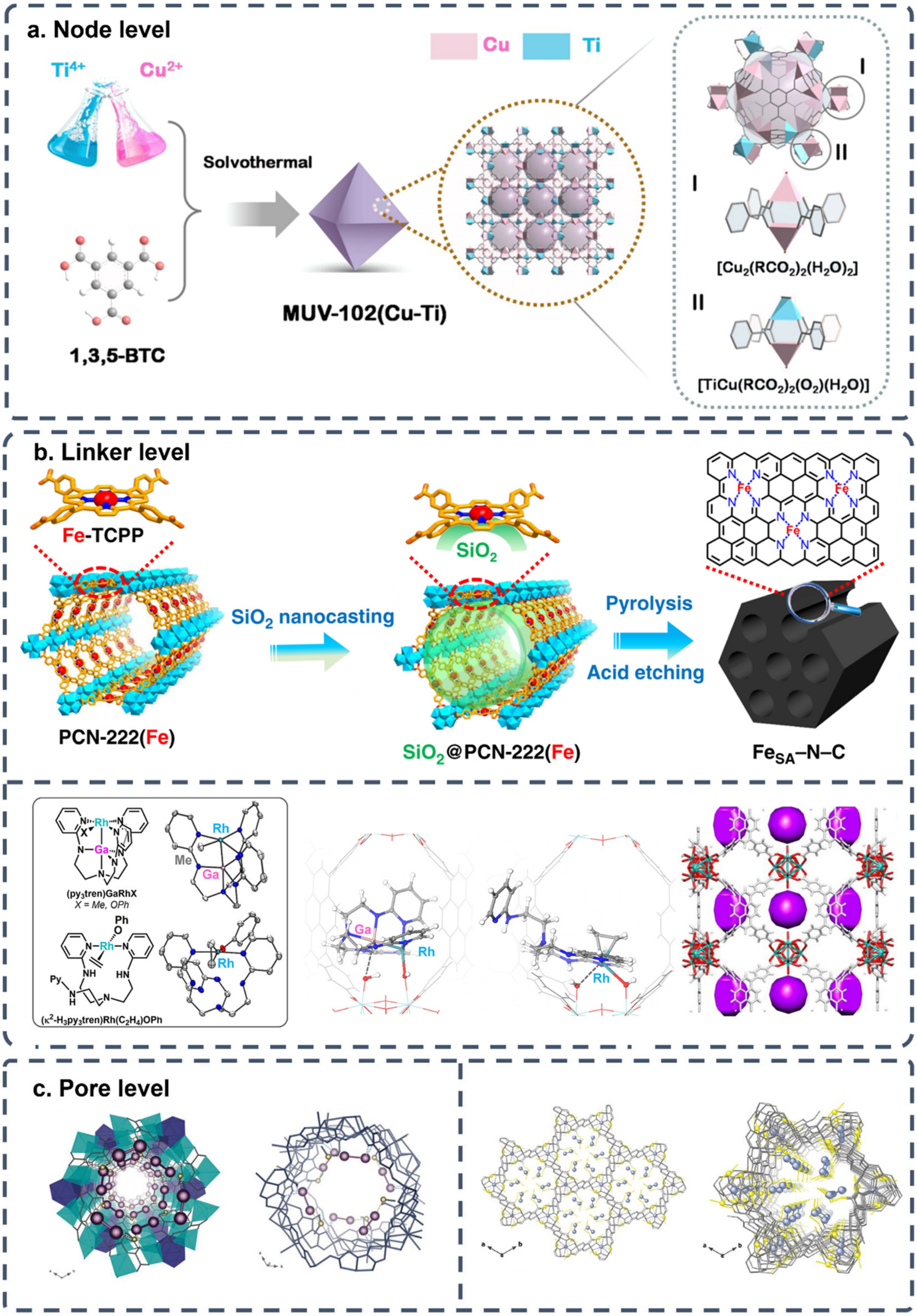

Fig. 3 (a) Structure of MUV-102(Cu–Ti) frameworks built from the interlinking of mono metal node Cu_2 and heterobimetallic TiCu clusters in MUV-102. Adapted from ref. 52 with permission from the American Chemical Society, copyright 2020. (b) Schematic of the nanocasting-enabled conversion of PCN-222(Fe) into FeSA–N–C (top). Adapted from ref. 54 under the Creative Commons CC-BY 4.0 license. Bottom: single-crystal X-ray structures of the RhGa and Rh (center) molecular precursors. Right: density functional theory (DFT)-optimized structures of the corresponding species confined within an ~8.5 Å pore. Adapted from ref. 55 with permission from the American Chemical Society, copyright 2018. (c) Left: perspective view of a channel of S-rich functional MOFs, dashed lines indicate Pt–S interactions, and the channel fragment highlighting framework interactions, where yellow dashed lines denote Pt–S bonds and blue dashed lines denote Pt–O contacts. (Cu, cyan; Ca, blue; S, yellow; Pt, purple; organic ligands, gray sticks.) Adapted from ref. 58 with permission from Wiley-VCH, copyright 2018. Right: fragment of Ag^0@thioether-functionalized MOFs, and view along the [111] direction. Adapted from ref. 59 under the Creative Commons CC-BY 4.0 license.

2.2.1.2 Linker level. Using the linker layer as a programmable unit, porphyrinic Zr-MOFs (TCPP linkers) encode inter-site spacing by arranging adjacent N_4 pockets in the lattice; once metalated, this registry can be carried through short-diffusion, low-mobility conversion into neighboring sites. Cichocka *et al.*[53] tuned the N_4-pocket separation in PCN-226 (a porphyrinic Zr-MOF) *via* chain-based inorganic building units, establishing linker-dictated control over $d_{M–M}$ and activity. Under a pore-assisted conversion window, Jiao *et al.*[54] nanocast SiO_2 into PCN-222(Fe) to provide dual protection during carbonization, thereby preserving linker-encoded single-site isolation at high loading and transferring it into Fe–N–C (Fig. 3b top).

Complementing this, Fig. 3b (bottom) illustrates the post-synthetic node grafting (low-temperature fixation) logic that avoids high-temperature rearrangements: heterobimetallic complexes are pre-assembled in solution and then grafted to Zr_6 nodes. Desai *et al.*[55] used a py_3tren scaffold to pre-assemble Rh–Ga, then anchored it onto NU-1000. Thompson *et al.*[56] grafted Co–Al(py_3tren) into NU-1000 (a Zr-based MOFs), quantifying up to one Co–Al set per Zr_6 node with uniform intracrystalline distribution, and showed that about 300 °C treatment decaps ligands without framework damage—opening a window for further inorganic fixation. Ponce *et al.*[57] directly grafted Ru–Ga using $[MeRu(\eta^6\text{-}C_6H_6)(PPh_3)_2][GaMe_2Cl_2]$ into NU-1000, establishing Ru : Ga ≈ 1 : 2, framework retention, and site stability, thereby demonstrating the generality and reproducibility of the pre-assembly to node anchoring strategy.

Together, linker programming pre-registers geometry and, under constrained conversion, transfers it with high fidelity to conductive hosts; both routes converge on node-directed, programmable co-location: one inherits $M–N_x$/$M–C_x$ anchors and forms pairs *via* sequential loading, and the other uses low-temperature coordination grafting to install two metals at a single, well-defined site.

2.2.1.3 Pore level. In the end, MOFs provide a direct route to program and preserve pore-confined adjacency: by confining metal precursors in the pores and then applying a mild reduction, one can maintain atomic dispersion while enriching near-neighbor yet non-metal–metal-bonded geometries even at comparatively high nominal loadings. Pardo's group[58] used a thioether-armed, S-rich functional MOFs as a soft channel wall: as shown in Fig. 3c (left), sulfur-rich functional MOFs channels stabilize Pt through an interwoven network of multi-point soft coordination and weak contacts. Pt^{2+} is quantitatively loaded *via* a double-solvent/capillary infiltration step and then gently reduced with $NaBH_4$ or dilute H_2. The synergy of pore-neck confinement and S anchoring generates, *in situ*, mutually proximal Pt_2^0 units/ultrasmall clusters that remain stable and efficient across several low-temperature industrial reactions—an explicit demonstration that pore-confined neighboring pairs with suppressed migration/sintering are both feasible and reproducible. In the same design logic, Zheng and co-workers[59] loaded Ag^+ into a related thioether-functionalized MOFs (Fig. 3c right) and used $NaBH_4$ reduction to isolate $Ag_2(0)$ dimers within the channels for CO_2-to-CH_4 hydrogenation, overcoming silver's strong tendency to aggregate and further validating the stabilizing role of soft-S pore walls and pore-neck geometry for a neighboring but non-bonded state. As a general process motif, the double-solvent method has also been established in UiO-66 (a Zr-based MOFs): Sun *et al.*[60] confined Pd^{2+} inside the cages of NH_2-UiO-66 and performed low-temperature reduction to afford less than 1.2 nm, pore-confined, highly dispersed Pd clusters/near-neighbor ensembles.

Extending this confinement-first logic to MOF-defined interfaces, Jiang *et al.*[61] built a core–shell ZIF-8@ZIF-67 nanocage, introduced Fe and Co precursors at the shell, coated with polydopamine as an N source, and then carbonized to inherit the prearranged nearest-neighbor statistics into the shell: the resulting nanocarbons displayed high-density neighboring Fe/Co $M–N_x$ sites fixed at the cage interface rather than arising from high-loading stochastic encounters, showing that MOFs pore/interfacial geometry can pre-bias adjacency and transfer it with fidelity during conversion. Finally, Zhu *et al.*[62] adopted a host–guest route to build Ni–Cu pairs: Ni partially replaced Zn in ZIF-8, and a Cu/1,10-phenanthroline complex was confined in the micropores. During pyrolysis, Zn evaporation together with spatial confinement suppressed aggregation and drove the formation of quasi-covalently coupled Ni–Cu pairs on N-doped carbon. HAADF-STEM resolved a projected inter-site spacing of about 2.4 Å, and EXAFS identified Ni–Cu scattering paths of about 2.03–2.05 Å. Taken together, a confinement-first followed by mild activation strategy enriches pore-localized near-neighbor metal sites, while pore-neck constriction and the intrapore coordination field limit migration.

2.2.2 COFs and 2D covalent polymers. COFs and 2D covalent polymers provide a lattice-programmable way to dictate how two metals sit next to each other and then hand that adjacency off to catalytically robust environments. Their value lies in (i) writing binuclear geometry directly into the repeating unit, (ii) using the framework's chelating pores to assemble two metals post-synthetically under confinement, and (iii) converting the preorganized polymers into conductive carbons while preserving rather than erasing the preset metal to metal neighborhood.

2.2.2.1 Lattice-encoded adjacency. At the lattice-encoded adjacency tier, Yang and co-workers[63] used nucleophilic aromatic substitution polymerization of octa-hydroxy metallophthalocyanines with tetrafluoroterephthalonitrile to build polyarylether-linked metallophthalocyanine sheets, so that nearest-neighbor metal spacing is directly written into a periodic 2D coordination lattice at the moment of polymerization. The chemically robust polyarylether backbone tiles planar, metalated macrocycles into a periodic in-plane grid, furnishing preset anchoring sites and fixed intersite spacing for subsequent binuclear placement. Along the same chemistry line, Yue *et al.*[64] co-polymerized two pre-metalated phthalocyanine monomers (Fig. 4a, $CuPcF_8$ and CoPc, Pc is phthalocyanine) *via* dioxin linkages to obtain bimetallic COFs, thereby encoding heterometal M^1/M^2 adjacency as a repeating lattice unit at the moment of polymerization—turning pairing from a high-temperature, stochastic encounter into a synthesis-controlled

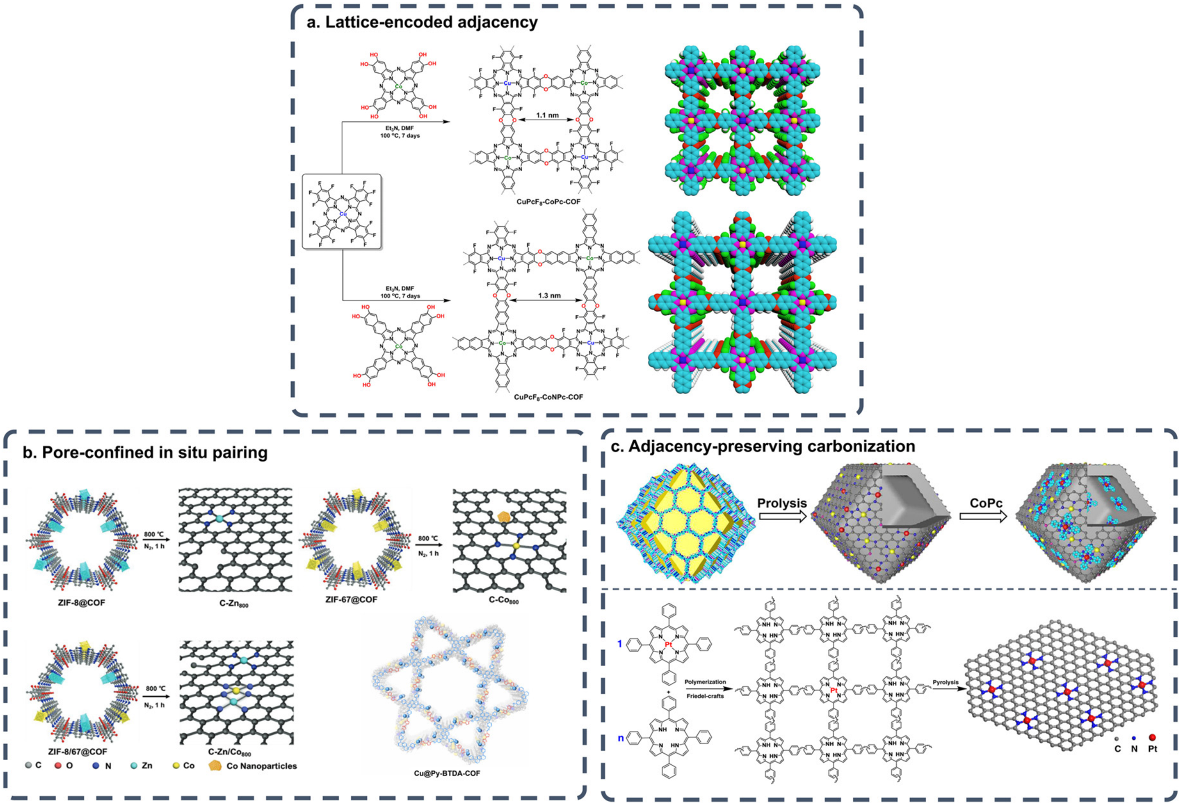

Fig. 4 (a) Schematic representation for the synthesis of $CuPcF_8$–CoPc–COF (top) and $CuPcF_8$–CoNPc–COF (bottom) under typical solvothermal conditions. (C, cyan; O, red; F, green; N, violet; Co, yellow; Cu, blue; H, white.) Adapted from ref. 64 with permission from the American Chemical Society, copyright 2021. (b) Schematic illustration of synthesis procedure of C–Zn_{800}, C–Co_{800}, and C–Zn/Co_{800} catalysts. Adapted from ref. 66 with permission from Wiley-VCH, copyright 2023. Bottom right: structural schematic of Cu@Py-BTDA-COF. Adapted from ref. 67 with permission from Elsevier, copyright 2025. (c) Top: synthesis of DACs from COFs@MOFs; bottom: schematic illustration of the preparation of Pt_1–N–C. Adapted from ref. 69 and 72 under the Creative Commons CC-BY 4.0 license.

construct. Complementing these experimental blueprints, Zhang *et al.*[65] employed a synthesized Cu–salphen COFs as a computational template and showed that its intrinsic double-vacancy cavities can stably host transition-metal dimers (Fe, Co, Mo, W, Ru). From this, they derived prescriptive site selection rules that map cavity size, coordination number, and admissible metals and provide a ready-to-use playbook for embedding dual-atom motifs directly within COFs lattices *via* lattice-encoded adjacency.

2.2.2.2 Pore-confined in situ pairing. At the pore-confined *in situ* pairing tier, COFs and 2D covalent polymers are used as nanoreactors for in-pore binuclear assembly: a framework bearing intrinsic N-donor pockets and uniform channels is first prepared, then a sequential load to coordination lock to mild activation cadence is applied so that two metals pair *in situ* within the same pore rather than by long-range diffusion. In a general protocol, Yang *et al.*[66] introduce two metal precursors stepwise into the framework's chelating sites and follow with a moderate anneal that allows only short-range migration and local re-coordination, thereby fixing adjacent M^1/M^2 sites in the pore rather than clusters (Fig. 4b, for the C–Zn_{800}, C–Co_{800}, and C–Zn/Co_{800} workflow). As a concrete and reproducible implementation of this logic, Chen *et al.*[67] target Cu pairs in an imine Py–BTDA COFs (Cu@Py-BTDA-COF): they first synthesize the Py–BTDA network, pre-coordinate Cu^{2+} to N sites, and then use gentle activation within the same pore domain to induce Cu–Cu dimers—the staged loading boosts the encounter probability while confinement suppresses agglomeration (Fig. 4b, bottom right), illustrating a prototypical pore-confined *in situ* pairing route. To further bias where pairing occurs and raise areal density, Yang *et al.*[68] propose a double-framework interface: assemble a COFs@MOFs heterojunction (defined as a core–shell construct in which a COFs shell is grown *in situ* on a MOFs core to form an atomically intimate interface), which load Co in the COFs and Zn in the MOFs, then apply a low-to-intermediate thermal program under which interfacial bonding/volatilization drives preferential nucleation at the interface; in practice they prepare ZIF-8 at room temperature, ultrasonically mix ZIF-8 with COFs monomers to build the COFs@MOFs composite, and complete programmed heat treatment, with the cooling segment identified as decisive for generating Co–Zn/Co–Co/Zn–Zn binuclear sites *via* interface-localized, pore-confined *in situ* pairing.

2.2.2.3 Adjacency-preserving carbonization. Adjacency-preserving carbonization of N- or N/P-rich COFs/2D covalent polymers into N-doped carbons offers a template-driven route to DACs. The polymer lattice pre-writes nearest-neighbor relationships between metal precursors, and low-mobility pyrolysis transcribes this lattice-encoded pairing into conductive carbon and fixes dual-atom motifs while minimizing migration and elemental loss. A representative core–shell implementation was reported by Liu *et al.*:[69] a COFs shell is grown on a ZIF-8 core (COFs@MOFs), followed by programmed carbonization to yield a heteroatom-rich hollow carbon; mild post-loading of Co phthalocyanine then secures adjacent ZnN_4 and CoN_4O sites on the same scaffold (Fig. 4c, top). The procedure exploits the COFs shell to suppress metal migration and elemental loss, while the MOFs core preserves architecture and porosity. In a complementary one-pot variant, Miao *et al.*[70] pre-install N/P coordination pockets in a COFs, introduce Fe, and rely on carbonization-induced rearrangement to generate Fe_2N_5P binuclear centers, exemplifying a template-guided, low-migration fixation of paired sites. As a compatible two-step alternative using covalent triazine frameworks precursors, Co is first embedded and pyrolyzed to form Co–N–C, after which Fe is introduced and a second pyrolysis affords neighboring Fe/Co sites,[71] again relying on adjacency-preserving carbonization to lock in proximal sites. In parallel, a conceptually consistent precursor-dilution polymer to N–C strategy[72] sets the average intersite statistics before carbonization by co-polymerizing metallotetraphenylporphyrins with metal-free tetraphenylporphyrin diluent and then pyrolyzing to N-doped carbon: the dilution ratio governs metal loading/dispersion such that atomically dispersed sites are obtained across 24 different metals, whereas removing the diluent leads to Pt nanoparticles under otherwise identical conditions (Fig. 4c, bottom). Across these routes, tuning the levers above preserves lattice-encoded adjacency, raises site density, and stabilizes the desired coordination environments through adjacency-preserving carbonization.

2.2.3 Other ordered supports. Beyond framework hosts (MOFs and COFs), ordered inorganic substrates can likewise write diatomic or neighboring single atom geometries directly at interfaces or hard surfaces and inherit them with high fidelity under mild reduction or carbonization. The operating principle is to use a hard ruler such as lattice periodicity, surface terraces, and pore necks to predefine nearest neighbor spacing; apply a soft ink such as N rich organic overlayers or gentle ligands to enforce sequential metalation and low mobility activation; and thus lock two metals in subnanometer proximity without coalescence rather than relying on high loading statistics.

2.2.3.1 Oxide substrates. Leveraging the lattice and terrace periodicity of oxides to define metal–metal spacing, and using N-rich overlayers or mild activation to control metalation and diffusion, oxide supports bring two metals into close proximity and then immobilize them under low-mobility conditions. Yan and co-workers[18] formalized an "interfacial-fixing" workflow that coats the oxide with polydopamine, sequentially adsorbs two metal precursors, pre-cures, pyrolyzes in N_2/NH_3, and finally selectively etches the oxide, thereby writing preset nearest-neighbor distances for homo- or heteronuclear $M–N_x$ pairs (M = Fe, Cu, Co, Ni, Zn, Mn) directly into the N-doped carbon shell; in Fe exemplars the fraction of neighboring Fe sites exceeded 95%, and the strategy is explicitly generalizable across metals (Fig. 5a). Building on the same logic with a specific oxide, Gu *et al.*[73] anchored adjacent single-atom Fe on MnO_2 *via* polydopamine coating/metal uptake and demonstrated that MnO_2-hosted Fe dimers arise and operate under oxidation conditions, indicating that proximity is encoded at the interface rather than achieved statistically at high loadings. In a lattice-encoded variant of the same principle, Liu *et al.*[74] used a self-limited cation-exchange on hexagonal $SrMnO_3$ followed by a mild 400 °C anneal to embed Ir into Mn sites and generate in-lattice Ir–Mn dual-atom units (Fig. 5b, Ir–Mn ≈ 2.41 Å). Beyond dense oxides, ordered aluminosilicate zeolites provide well-defined crystalline micropores, where a hierarchical ultra-stable Y-type aluminosilicate zeolite with bimodal micro/mesoporosity is used as the scaffold and 2-methylimidazolate serves as an in-pore bridging ligand, Chen *et al.*[75] modularly assembled Cu–M dual-atom sites (M = Co, Ni, Zn) without carbonization; EXAFS resolved two crystallographic metal sites about 5.8 Å apart with only first-shell M–N/O scattering.

On the model $Fe_3O_4(001)$ surface, Meier and colleagues[76] patterned sub-nanometer Pt_2 neighbors at ultralow dose and mild activation, showing that metastable dimers facilitate lattice-oxygen extraction in CO oxidation and that terrace periodicity can act as a geometric stencil without driving agglomeration. Complementarily, Wang *et al.*[77] mapped the CO-induced dimer-decay window on a model single-atom platform, underscoring that coverage/temperature/atmosphere must be co-tuned to preserve neighboring yet non-metal–metal-bonded geometries; CO can drive sintering to stable $Pt_2(CO)_2$ species that only split upon heating, and diffusion barriers of carbonyl intermediates can outcompete reaction barriers—practical guidance for retaining adjacency without coalescence under reactive gases.

2.2.3.2 Carbon-based ordered supports. Relative to oxide/framework hosts, carbon-based ordered supports also make diatomic/neighboring single-atom sites a programmable synthesis problem. At one end, polymeric carbon nitride enables geminal pre-assembly: Hai *et al.*[78] positioned two Cu atoms in adjacent N_4 pockets and, under mild activation, allowed the pair to approach and separate reversibly during turnover (forming/cleaving a Cu–Cu bond). In this scheme, adjacency is written directly by pocket geometry and maintained without permanent M–M bonding, providing a clean, carbon-based semiconductor window for reversible proximity. In parallel, Z. Chen *et al.*[79] established sequence-locked pairing on framework-free N-doped carbon: Fe is anchored first to make $Fe–N_x$, a second metal (Fig. 5c, Fe or Mn) is introduced second, and a low-mobility anneal permits only short-range rearrangement, thereby fixing adjacent Fe–Mn sites in the same pore domain. The same Fe to M order ports to Fe–Co, Fe–Ni, and related

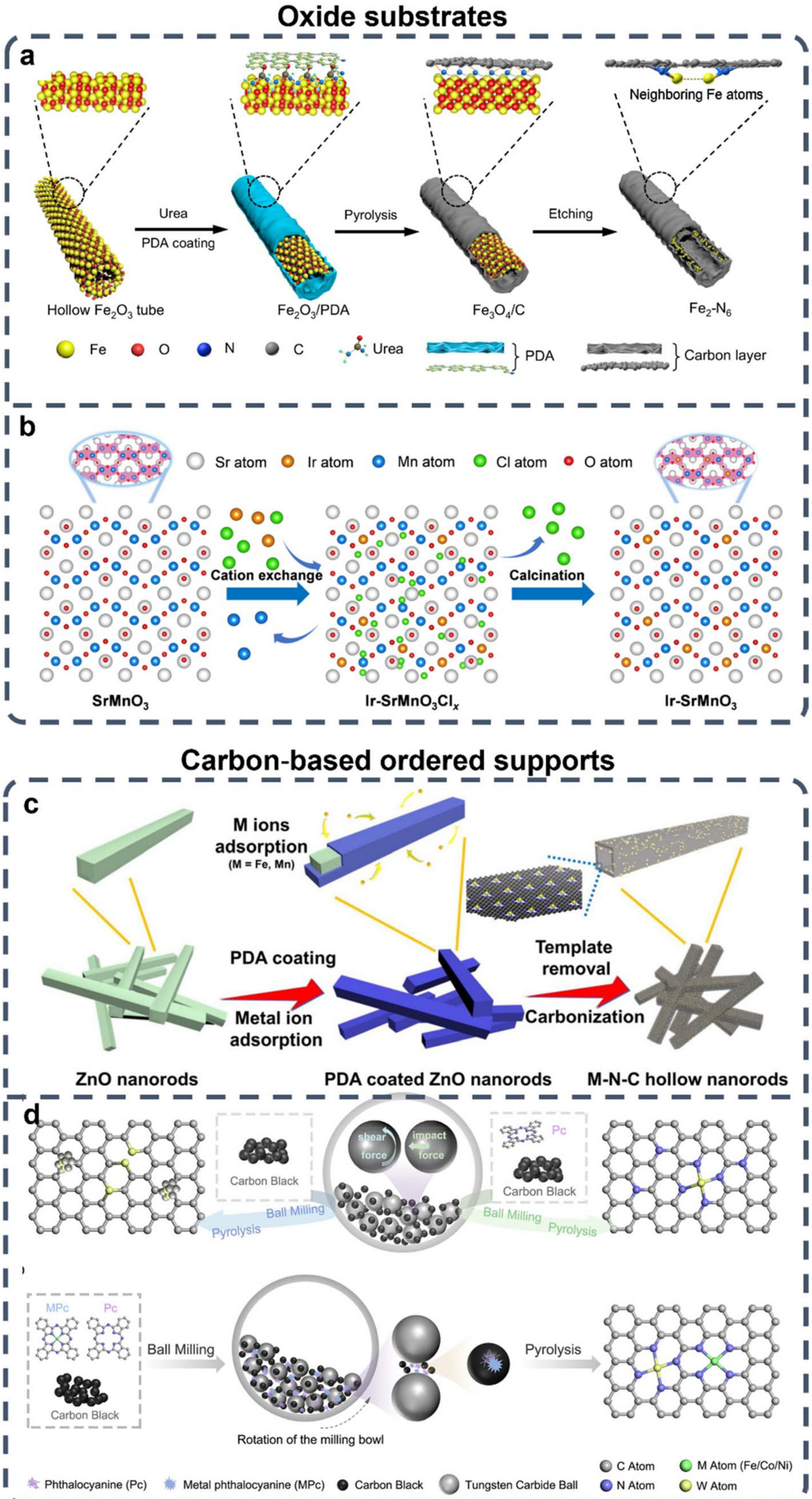

Fig. 5 Schematic illustration of the synthesis of (a) Fe_2–N_6. Adapted from ref. 18 under the Creative Commons CC-BY 4.0 license; and (b) Ir-$SrMnO_3$. Adapted from ref. 74 with permission from Wiley-VCH, copyright 2024. (c) Schematic illustration of the formation process of M–N_x–C hollow nanorods. Adapted from ref. 79 with permission from Elsevier, copyright 2021. (d) First, a tungsten-carbide nanoparticle–carbon black catalyst and single-atom W–N–C are produced by stripping W atoms from tungsten-carbide milling balls; then, 3d–5d hybrid diatomic M,W–N–C catalysts (M = Fe, Co, or Ni) are prepared by co-introducing an exogenous N-containing complex and a 3d-metal complex into the starting mixture. Adapted from ref. 80 under the Creative Commons CC-BY 4.0 license.

pairs by swapping the second metal while preserving orthogonal coordination and the thermal window. For scalable practice, Li and co-workers[80] coupled mechanochemistry with single-step heat setting (Fig. 5d): ball-milling carbon black with Pc/FePc brings molecular precursors into intimate contact, while the Pc N_4 pocket captures W abraded from the milling media; a single anneal then yields neighboring Fe–N_4/W–N_4 sites. This solvent-lean route generalizes to M_1–N_4/W–N_4 families and demonstrates that polymeric carbon nitride's geminal, reversible adjacency and N-doped carbon's sequence-locked, low-migration fixation can be integrated into a coherent, carbon-based playbook, turning near neighbor from a statistical accident into a synthesis pathway jointly tuned by geometry, sequence, and the thermal window.

2.3 Molecular engineering—multinuclear metal–organic complex

Molecularly programmable and inheritable in the solid state, MOCs provide deterministic blueprints for constructing DACs.[81] Through ligand-field design, MOCs predefine the interatomic separation d_{M-M}, primary coordination number, and the accessible oxidation-state window, while bridging motifs (μ-O/μ-S/μ-X; carboxylates; halides; diphosphine/diamine linkers, among others) pre-organize paired metal sites at the molecular scale.[82,83] During immobilization followed by low-temperature, stepwise de-ligation/controlled thermolysis, this predefined geometric and electronic configuration is transferred to N/O/S/P donor sites on the support, locking adjacent M^1/M^2 motifs with prescribed d_{M-M}. In contrast to high-temperature, chance-encounter aggregation, the MOCs route enables deterministic homo- or heteronuclear pairing, tunable d_{M-M} and coordination environments, and reproducible batch to batch synthesis, thereby advancing diatomic sites from concept and serendipity to a programmable, verifiable, and scalable materials strategy. Based on these considerations, Table 1 summarizes representative MOCs precursors for DACs and lists their molecular structures, highlighting ligand frameworks and bridging groups to facilitate quick structural comparison. Although the main body of this Review focuses on diatomic motifs, this section also discusses selected triatomic complexes as natural extensions of the same blueprint chemistry; for clarity, such species are referred to as TACs rather than DACs in the strict sense.

2.3.1 Carboxylate bridges. Based on their structural features, MOCs for building DACs and TACs can be categorized into four classes: carboxylate-bridged, metal carbonyl cluster compounds, heteroatom-bridged dinuclear complexes, and π-ligated & macrocyclic scaffolds. Carboxylate bridges exploits the molecularly preset geometry of paddlewheels/low-nuclear acetates and transfers it to the solid *via* a preset geometry to handover sequence. A canonical example is the paddlewheel $Rh_2(OAc)_4$/MgO system, where acetate exchange and Rh–O (surface) coordination generate adjacent Rh pair-sites that can be steered—by atmosphere and temperature—either to persist as paired Rh–Rh motifs or to cleave into isolated Rh atoms (ethylene hydrogenation as a sensitive probe).[84] Applying the same logic to Cu and Pd yields analogous outcomes: $Cu_2(OAc)_4$ immobilized on N-doped carbon undergoes stepwise deacetylation and re-coordination into Cu_2–N_x pairs that promote C–C coupling in CO_2 electroreduction, delivering C_2 products with selectivity unattainable on Cu_1 sites.[85] Likewise, $[Pd(OAc)_2]_3$ on exfoliated g-C_3N_4 undergoes moderate deacetylation and *in situ* capture by closely spaced N sites, enabling programmable divergence between Pd_1 and adjacent Pd–Pd by tuning N-site density, ramp rate, and atmosphere strength.[86] Building directly on this "preset geometry to handover" logic, Wei *et al.*[87] combined acetate-type ligand stripping with heteroatom-modulated hosts to bias pair retention: isostructural trinuclear $Fe_2Zn/Fe_2Co/Fe_3$ complexes ($[Fe_2Zn(\mu_3\text{-}O)(O_2C\text{-}t\text{Bu})_6(H_2O)_3]/[Fe_2Co(\mu_3\text{-}O)(O_2C\text{-}t\text{Bu})_6(H_2O)_3]/[Fe_3(\mu_3\text{-}O)(O_2C\text{-}t\text{Bu})_6(H_2O)_3]$) were first immobilized on MOF-derived graphitized N-carbons; gentle thermolysis then synchronized ligand removal with simultaneous capture by adjacent donor pairs, suppressing aggregation and delivering Fe–Fe dual-atom and Fe_3 triatomic endpoints. Similarly, Tang *et al.*[88] used a pre-assembled Co_3 complex (Co_3L) as the metal source, ultrafast-printing it into graphene nanosheets followed by a short, mild consolidation to preserve a Co_3–N–C triatomic motif. Taken together, these works position carboxylate-bridged dimers as versatile, programmable precursors that can be directed—*via* atmosphere and thermal schedule—to either dual-atom or single-atom endpoints with reproducible control.

2.3.2 Metal carbonyl cluster compounds. Unlike carboxylate bridged systems that preset a geometry for handover, metal carbonyl cluster compounds follow a preserve the core and shed the shell logic. The cluster core retains the intrinsic metal–metal topology, while the CO shell can be removed stepwise at relatively low temperatures, with terminal CO ligands dissociating before μ-CO. Practically, the intact cluster is first immobilized under anhydrous, oxygen-free conditions onto supports rich in adjacent donor pairs/multiplets. A subsequent, narrow-window decarbonylation allows surface N/O/S sites to take over coordination before metal migration, thereby transplanting the molecular nuclearity directly onto the solid surface. This structure-to-process logic is validated across systems: $Fe_2(CO)_9$ supported on g-C_3N_4 is grafted intact and then subjected to mid-temperature removal of terminal CO (retaining μ-CO until re-coordination is complete) to lock in Fe_2 for alkene epoxidation;[89] Tian *et al.*[90] precisely dosed $[(\eta^5\text{-}C_5H_5)Fe(CO)_2]_2$ undergo staged thermolysis, with site-density and atmosphere programming tuning the number of Fe atoms per site to match acidic ORR demands; and $Ru_3(CO)_{12}$ supported on defect-rich and N-rich carbons can be anchored at low temperature and mildly decarbonylated to freeze a Ru_3 TACs for electrochemical sensing.[91]

2.3.3 Heteroatom-bridged dinuclear complexes. In heteroatom-bridged dimers, the bridge itself (μ-O/μ-OH/μ-S/μ-X, or chelating N/P donors) pre-organizes two metal centers and then hands them off to adjacent donor pockets on a solid during mild activation. A representative *in situ* μ-oxo strategy photochemically generates Ir_2 sites on metal–oxide supports: two Ir from $[Ir(pyalc)(H_2O)_2(\mu\text{-}O)]_2^{2+}$ cations are assembled and

Table 1 A summary of MOCs as programmable precursors for building DACs and TACs

Ref.	Type	Constitutional formula	Common name	Support
84	Carboxylic acid bridged	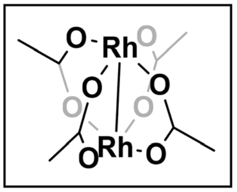	$[Rh_2(OAc)_4]$	MgO
85	Carboxylic acid bridged	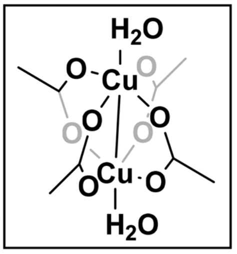	$[Cu_2(CH_3COO)_4 \cdot 2H_2O]$	N-doped carbon
86	Carboxylic acid bridged	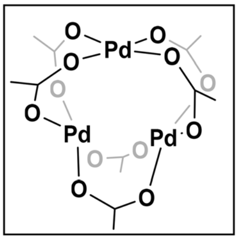	$[Pd(OAc)_2]_3$ (palladium acetate trimer)	Exfoliated graphitic carbon nitride
87	Carboxylic acid bridged	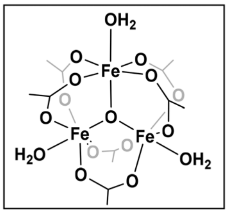	$[Fe_3(\mu_3\text{-}O)(O_2C\text{-}t\text{Bu})_6(H_2O)_3]$	Graphitized nitrogen-doped carbon layer
87	Carboxylic acid bridged	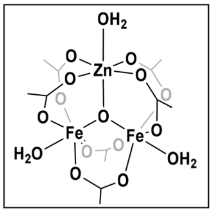	$[Fe_2Zn(\mu_3\text{-}O)(O_2C\text{-}t\text{Bu})_6(H_2O)_3]$	Graphitized nitrogen-doped carbon layer
87	Carboxylic acid bridged	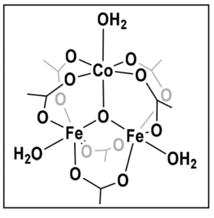	$[Fe_2Co(\mu_3\text{-}O)(O_2C\text{-}t\text{Bu})_6(H_2O)_3]$	Graphitized nitrogen-doped carbon layer
88	Carboxylic acid bridged	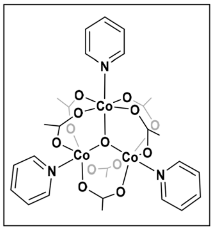	Co_3L	N-doped graphene

Table 1 *(Contd.)*

Ref.	Type	Constitutional formula	Common name	Support
89	Metal carbonyl cluster compound	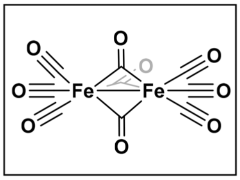	$[Fe_2(CO)_9]$	ZIF-8
90	Metal carbonyl cluster compound	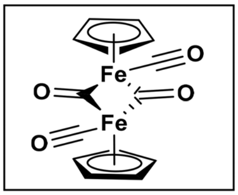	$[(\eta^5\text{-}C_5H_5)Fe(CO)_2]_2$ (bis(dicarbonyl (η^5-cyclopentadienyl)iron))	Mesoporous carbon nitride ($g\text{-}C_3N_4$)
91	Metal carbonyl cluster compound	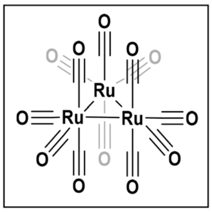	$[Ru_3(CO)_{12}]$	ZIF-8
92	Heteroatom-bridged dinuclear complex	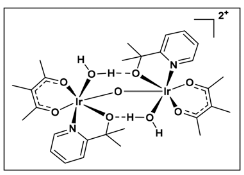	$[Ir(pyalc)(H_2O)_2(\mu\text{-}O)]_2^{2+}$	$\alpha\text{-}Fe_2O_3$
93	Heteroatom-bridged dinuclear complex	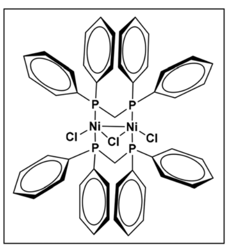	$[Ni_2(dppm)_2Cl_3]$	ZIF-8
86 and 90	Heteroatom-bridged dinuclear complex	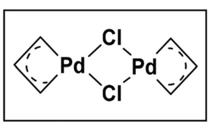	$[PdCl(\eta^3\text{-}C_3H_5)]_2$ (allyl palladium chloride dimer)	Graphitic carbon nitride
94	Heteroatom-bridged dinuclear complex	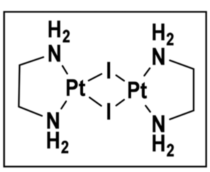	$Pt_2(\mu\text{-}I)_2(en)_2$ (ethylenediamine)iodo-platinum(II) dimer dinitrate	Graphitic carbon nitride
90	Heteroatom-bridged dinuclear complex	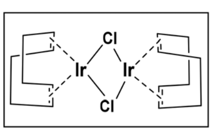	$[IrCl(COD)]_2$ (chloroiridium-cycloocta-1,5-diene)	Graphitic carbon nitride

Table 1 *(Contd.)*

Ref.	Type	Constitutional formula	Common name	Support
95	Heteroatom-bridged dinuclear complex	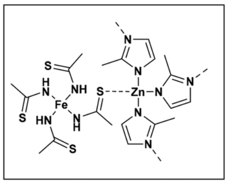	$[FeN_3–S–ZnN_3]$	ZIF-8
96	π-Ligated & macrocyclic scaffolds	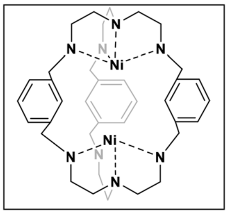	Dinuclear nickel cryptate	Carbon black
97	π-Ligated & macrocyclic scaffolds	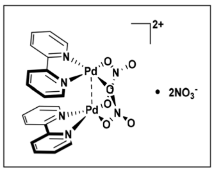	Palladium(II) nitrate hydrate (anion replacement deposition–precipitation)	Acetylene black
98	π-Ligated & macrocyclic scaffolds	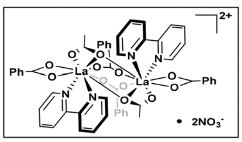	$[La_2(BA)_4(NO_3)_2(phen)_2]$	Graphene oxide
99	π-Ligated & macrocyclic scaffolds	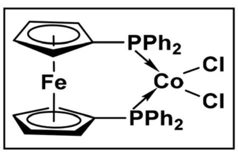	d [1,1′Bis(diphenylphosphino) ferrocene]cobalt(II) ($C_{34}H_{28}Cl_2CoFeP_2$)	ZIF-8
100	π-Ligated & macrocyclic scaffolds	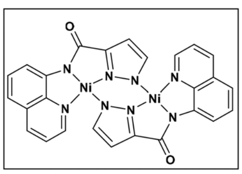	$[Ni_2(qpyzc)_2]$	CNTs
101	π-Ligated & macrocyclic scaffolds	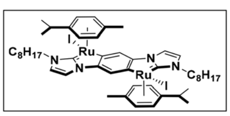	[Ru]–benzene	CNTs
101	π-Ligated & macrocyclic scaffolds	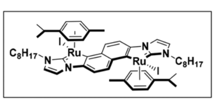	[Ru]–naphthalene	CNTs
102	π-Ligated & macrocyclic scaffolds	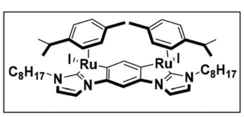	[Ru]–*m*-benzene	CNTs
83	π-Ligated & macrocyclic scaffolds	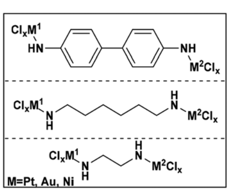	Dinucleating diamine ligand	$g-C_3N_4$

Table 1 *(Contd.)*

Ref.	Type	Constitutional formula	Common name	Support
103	π-Ligated & macrocyclic scaffolds	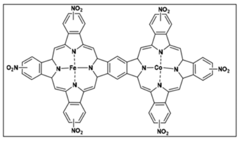	Bimetallic phthalocyanines macromolecules (FeCoPc)	ZIF-8
104	π-Ligated & macrocyclic scaffolds	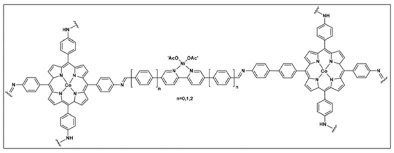	CoTAPP-Ni-n-2DP	—
88	π-Ligated & macrocyclic scaffolds	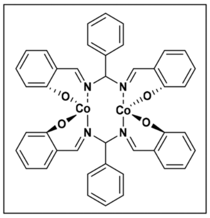	Co_2-L	N-doped graphene
105	π-Ligated & macrocyclic scaffolds	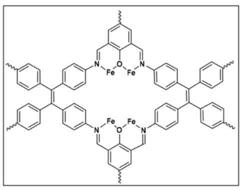	Fe_2-COFs	Hollow-structured COFs with preorganized bimetallic chelating sites (P-COFs)
106	π-Ligated & macrocyclic scaffolds	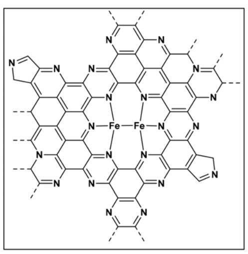	C_2N–Fe	—
107	π-Ligated & macrocyclic scaffolds	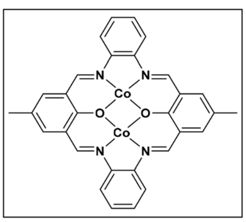	Co_2 complex	Ketjen black
108	π-Ligated & macrocyclic scaffolds	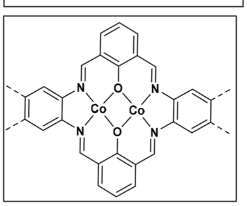	CoCo-BiSalphen	Ketjen black

O-bridged directly on α-Fe_2O_3, yielding a robust dinuclear motif without high-temperature reconstruction.[92] A complementary pre-bridged in molecules, then fix on N–C approach starts from diphosphine-bridged $Ni_2(dppm)_2Cl_3$; immobilization on N-doped carbon followed by staged ligand removal gives an atomically precise Ni_2 site in which the two Ni centers share nearby N donors forming a heteroatom bridged dinuclear environment on the support.[93] $[PdCl(\eta^3\text{-}C_3H_5)]_2$,[86,90] $Pt_2(\mu\text{-}I)_2(en)_2$,[94] and $[IrCl(COD)]_2$[90] are prototypical halide-bridged dimers that, upon impregnation onto exfoliated g-C_3N_4 or

N-doped carbons and a brief, mild activation, readily deliver the corresponding dual-atom catalysts. Finally, a bifunctional ligand assisted scheme uses an organic scaffold to preset the spacing between two different metals, Fe and Zn forming ([FeN_3–S–ZnN_3]), before fixing them on carbon. Tuning the donor framework controls the heterometallic d_{M-M} (about 3 Å) and stabilizes the bridged pair under ORR conditions.[95] This also represents one of the few approaches to heteronuclear dual-atom catalysts that proceeds *via* MOCs. Taken together, the common playbook is clear: preinstall a heteroatom bridge at the molecular level, immobilize the dimer on a donor rich support, and apply low temperature, stepwise ligand release so that surface N/O/S/P donors cooperatively capture and lock the pair, yielding durable M–(heteroatom)–M linkages or adjacent N/O anchored dinuclear sites featuring a predefined interatomic geometry.

2.3.4 π-Ligated & macrocyclic scaffolds. π-Ligated & macrocyclic scaffolds excel by combining large conjugation, strong interfacial interactions, and modular tunability. First, extended π backbones (porphyrins/phthalocyanines, η^6-arenes, Cp/Cp*, *etc.*) engage graphitic and N-rich supports through π–π stacking and face–face adsorption, enabling uniform immobilization under mild conditions and suppressing metal migration/sintering during ligand release to re-coordination. This helps preserve the preset M^1/M^2 separation and orientation as molecular geometry is handed over to the solid. This logic is borne out by concrete molecule/support pairs. A dinuclear nickel cryptate (a cryptand-based macrocycle that chelates two Ni and pre-sets the Ni–Ni separation) immobilized on carbon black transfers its dimeric geometry intact after gentle de-ligation, giving adjacent Ni pairs.[96] Palladium(II) nitrate hydrate on acetylene black exploits the lability of nitrate/water ligands together with π-rich carbon domains to place two Pd species side-by-side and lock them as neighboring Pd_2–C/N_x sites under a brief, mild activation.[97] Sun *et al.*[98] employed a pre-paired binuclear La complex, [$La_2(BA)_4(NO_3)_2(phen)_2$], embedded in N-doped graphene. Ultrafast Joule heating cleaves the dimer *in situ* while NH_3 supplies reactive nitrogen, transferring the preset La–La geometry into a stable La_2–N_6 site. d [1,1′Bis(diphenylphosphino)ferrocene]cobalt(II) confined in ZIF-8 uses a rigid ferrocene–bisphosphine bridge to maintain a dinuclear arrangement that is handed to the MOF pore surface upon gentle treatment, illustrating how π-rigid, chelating backbones preserve Fe–Co proximity in the solid.[99] A rigid multi-N bridged dimer, [$Ni_2(qpyzc)_2$], supported on Carbon Nanotubes (CNTs), hard-codes the Ni–Ni spacing within its aromatic linker; stepwise ligand removal then cleanly re-coordinates an atomically precise Ni_2–N_x site.[100]

Second, these scaffolds are organically programmable: substituents, bridge lengths, donor sets (N/P/S), pore size, and rigidity can be tuned to continuously adjust d_{M-M} (typically ~2.4–9.3 Å), electronic structure, homo/hetero-nuclear pairing, pocket polarity, and steric environment. In the conjugated planar molecules, [Ru]–benzene, [Ru]–naphthalene,[101] and [Ru]–*m*-benzene[102] act as planar π templates that encode Ru–Ru spacing at the molecular stage. Changing the arene (ring size/topology, *meta* substitution) presets distinct single-atomic interdistances (6.2/7.0/9.3 Å). These fragments co-adsorb on CNTs sidewalls *via* π–π stacking, and under mild ligand-release to re-coordination the arene is removed, preserving in the solid the Ru–Ru spacing that was programmed at the molecular stage; Besides, Ma and co-workers[83] used a dinucleating diamine ligand on g-C_3N_4 to preset metal adjacency and, after mild activation, transfer it to adjacent M–N_x; ethylenediamine, 1,6-hexanediamine, and 4,4′-diaminobiphenyl set Pt–Pt spacings of 2.2/4.7/>8.1 Å, and the same route yielded heteronuclear Pt–Au and Pt–Ni pairs with high pairing ratios; A cofacial metallophthalocyanine dimer (FeCoPc),[103] in which an Fe–Pc and a Co–Pc macrocycle are linked by a short N-donor bridge, pre-sets the Fe–Co separation and orientation at the molecular level, thereby enabling atomically precise control of the heteronuclear Fe–Co site. In the CoTAPP-Ni-n-2DP polymer series, tuning the linker length and conjugation modifies the Co–Ni spacing and coupling while keeping the active-center identity unchanged.[104] In the same spirit, the π-conjugated Co_2–L dimer ($C_{42}H_{32}Co_2N_4O_4Cl$) on N-doped graphene uses a short aromatic bridge with O/N donors to delimit the Co–Co distance, allowing mild schedules to lock uniform Co_2–N_x neighbors; paired with a preassembled Co_3 precursor, this system demonstrates selectable nuclearity within the same π-ligated design space.[88]

Third, preorganized frameworks, including COFs, ladder-polymer macrocycles, and dual-pocket macrocycles, encode the bimetal geometry at the molecular stage and, thanks to solution processability (coating, impregnation, confined growth), hand it off intact to solids under mild ligand-release to re-coordination, thereby replicating isostructural dual sites at high density. Representative pairs illustrate the logic: in Fe_2-COFs embedded in a P-COFs host, each COFs node carries a pair of preorganized chelating cavities held at a fixed separation by the rigid, conjugated linker. Impregnation and removal of labile auxiliary ligands place one Fe in each cavity, generating an array of Fe–Fe pairs with node-defined spacing, and this occurs without backbone reconstruction under the stated mild conditions;[105] By contrast, in C_2N–Fe, the triazine-type N arrays define periodically spaced donor pockets on the basal plane; introducing a molecular Fe precursor and then low-temperature de-ligation allows two neighboring pockets on the same rim to simultaneously bind two Fe centers, fixing them on adjacent lattice sites as Fe_2–N_x (correlated dual) sites rather than isolated Fe_1.[106] On the molecular dimer side, a well-defined Co_2 complex on Ketjen black leverages pre-existing Co–Co proximity (multidentate N/O) so that mild de-ligation lets neighboring donor pockets cooperatively "catch" an isostructural Co_2–N_x site,[107] while CoCo-BiSalphen on Ketjen black uses a planar, strongly conjugated bis-salphen macrocycle to lock Co–Co distance and angle, enabling high-areal-density Co_2 after gentle reorganization.[108]

Taken together, strong π anchoring plus a low-temperature de-shelling window, layered on top of broad synthetic modularity, make π-ligated and macrocyclic scaffolds a highly extensible platform for the controlled, precise construction of DACs, readily extendable, when desired, to triatomic motifs.

3. Effects of diatomic catalysts

Adjacency in DACs enables cooperative reaction pathways that are not accessible on fully isolated sites. In this section, we summarize these effects as three mechanism-oriented themes (Fig. 6). First, electronic-structure regulation: tuning d_{M-M}, nuclearity, and the ligand field retunes charge distribution, orbital hybridization, and spin polarization. Second, synergistic adsorption and activation: distance-matched two-center geometries enable bridged binding, preorganization, and pathway steering. Third, tandem effects: near-neighbor sites partition early and late steps and hand off intermediates in place, mitigating activation–release trade-offs and expanding operating windows.

3.1 Regulating electronic structure

DACs constitute a natural testbed for electron–geometry coupling.[16] By tuning d_{M-M}, nuclearity (homo- *vs.* heteronuclear), and the ligand-field strength of the anchoring environment (donor set and covalency, coordination number/geometry, and axial ligation), one can co-manipulate the three principal axes of the active site's electronic structure—charge distribution, orbital density/symmetry, and spin state/exchange splitting—within a single, programmable platform.[16,109] These levers are not independent toggles but a strongly coupled system: cross-site charge redistribution reshapes local electric and ligand fields, thereby shifting the d-band center and inducing orbital hybridization;[21,62,110] subtle orbital-level adjustments, in turn, feed back into spin-channel occupancy and exchange coupling; and spin polarization and selection rules directly govern rate-determining steps (RDS) in multielectron reactions.[111,112] When this triad is brought into register, key intermediates bind just right, transition-state barriers decrease, and catalytic performance is driven toward the Sabatier optimum.[110] For d_{M-M}, electronic and magnetic coupling peak within a narrow window ($Fe-N_4$ architectures for ORR often maximize intrinsic Turnover Frequency (TOF) at about 0.7–0.9 nm[17]); shortening further risks direct M–M bonding or reconstruction, whereas lengthening weakens coupling and erodes multi-center advantages.[40,113] For nuclearity or identity, homonuclear pairs enable symmetric two-center activation but can over-strengthen binding and narrow operating windows, while heteronuclear pairs introduce level or electronegativity offsets that moderate binding and permit role differentiation and short-range handoff.[21,46,62,110] For ligand-field strength, weak fields under-stabilize activated states and limit charge transfer, whereas overly strong fields over-stabilize bound states and damp inter-site coupling. Axial or second-shell coordination provides a practical handle to tune these effects in $M-N_4$

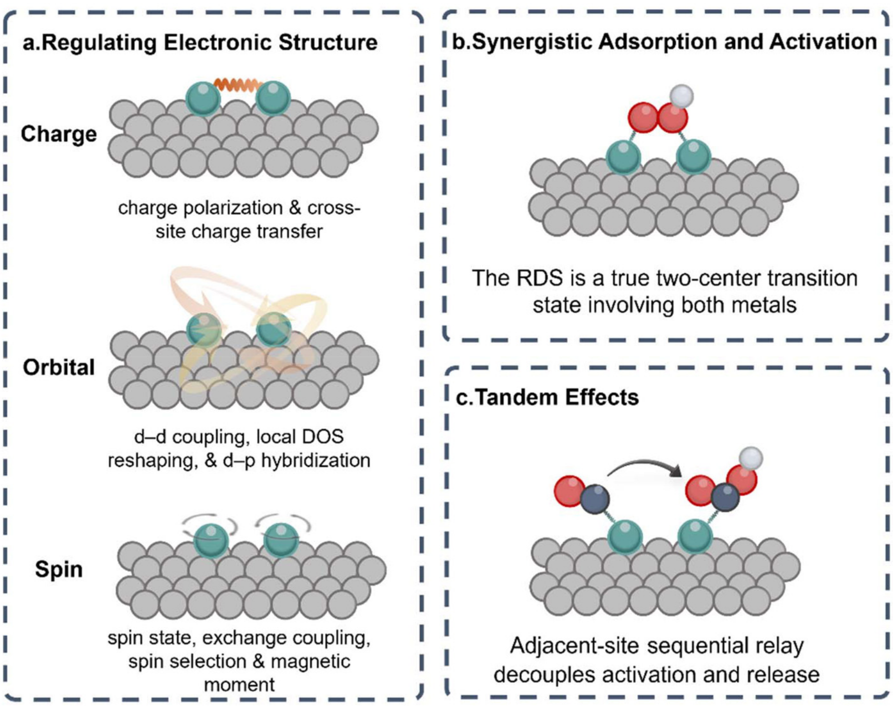

Fig. 6 Summary of DACs effects. (a) Å-scale proximity enables three coupled levers for electronic-structure regulation: charge polarization and cross-site transfer, d–d orbital coupling with local DOS reorganization, and spin-state tuning with exchange coupling. (b) Synergistic adsorption and activation, where the rate-determining transition state genuinely spans both metal centers. (c) Tandem effects on adjacent sites, in which sequential activation and product release are partitioned over different centers, mitigating the typical activation-release trade-off of single-site catalysts.

motifs.[114–116] Designing DACs therefore entails encoding a target triplet (d_{M-M} nuclearity/identity, ligand-field strength) into the material so that geometry, orbital matching, charge redistribution, and spin coupling are co-registered rather than merely coexisting.

3.1.1 Charge (polarization and cross-site transfer). Heteronuclear diatomic sites combine offsets in work function/electronegativity with mixed coordination shells, a combination that readily drives cross-site charge transfer and generates directional local polarization fields. In the Fe–Ni archetype for electrochemical CO_2 reduction, *operando* spectroscopy together with DFT indicate an electronic leveling of a redistribution of charge between the two centers: Fe's originally excessive binding strength is reduced while Ni's capability to activate intermediates increases. This rebalanced electronic structure lowers the barrier for *COOH formation and mitigates *CO over-binding, which in turn widens the potential window for selective CO production.[46] Extending this logic to Ni–Cu pairs, charge redistribution correlates quantitatively with interatomic spacing through a $|\Delta e|$–d_{M-M} relationship, where $|\Delta e|$ is the magnitude of inter-site charge transfer between the two metal centers. Shorter separations strengthen intersite polarization and charge transfer, promote *COOH formation, suppress the hydrogen evolution reaction (HER), and yield higher TOF and CO selectivity.[62] A closely related, support-mediated charge-redistributive synergy is observed in Fe–Co dual single-atom systems for oxygen electrocatalysis:[117] despite the absence of direct M–M scattering (isolated $Fe–N_4$/$Co–N_4$), co-doping downshifts the d-band centers and tunes adsorption energetics; DFT and free-energy analyses further reveal a functional partition, with $Fe–N_4$ favoring ORR and $Co–N_4$ favoring OER, and reduced overpotentials compared to the single-metal counterparts, evidencing charge-leveling type cooperation without direct pairing. Beyond electrocatalysis, neighboring Pd single atoms in thermocatalytic hydrodehalogenation outperform both isolated atoms and nanoparticles because the second Pd center provides charge compensation and polarization stabilization along a two-center pathway—an archetypal manifestation of charge-assisted diatomic cooperation.[31]

3.1.2 Orbital (d–d orbital coupling, local DOS reorganization and d–p hybridization). Placing two metals in controlled proximity induces d–d orbital coupling that shifts the d-band center and reorganizes the local DOS, thereby refining intermediate binding in accordance with the Sabatier principle. This effect operates in both homo- and heteronuclear pairs. For Fe–Fe or Fe–Ni sites, coupling narrows the bonding–antibonding gap for CO adsorption, mitigating the over-binding that limits $Fe–N_4$-type SACs.[29] In Ni–Cu pairs,[62] *COOH adsorption is primarily governed by Ni 3d–C 2p hybridization. The adjacent Cu modifies the electronic structure of Ni by shifting its 3d states closer to the Fermi level. This adjustment strengthens activation without causing overbinding. As a mechanistic analogue beyond electrocatalysis, Fe–Cu dual single-atom pairs on ZIF-8–derived N-doped carbon exhibit configuration-dependent d-band-center coordination:[118] nearest-neighbor $Fe–Cu–N_6$ sites favor a bilateral adsorption pathway with coordinated d-band center realignment of Fe and Cu, leading to moderated binding and lower barriers, whereas second-neighbor $Fe–Cu–N_8$ sites revert to one-side adsorption with higher barriers. As a distance-programmed analogue that lacks direct M–M bonding, correlated single-atom Ru systems reveal a negative correlation between intersite spacing and the Ru d-band center. Tuning the average spacing to ~7.0 Å programs long-range interactions that downshift the Ru d-band center to an optimal position, redistribute d-orbital occupation, and strengthen d–p coupling to adsorbates, thereby reorienting adsorption geometries and lowering transition-state barriers.[101]

3.1.3 Spin (spin state, exchange coupling, spin selection and magnetic moment). Spin control is a core lever of electronic-structure regulation. Exchange coupling between proximate centers—ferro- or antiferromagnetic and typically decaying with the inter-metal spacing—together with the ligand-field strength of N_4/N_x motifs, sets spin multiplicity, exchange splitting, and the spin-resolved DOS; this in turn dictates which spin channels are available to adsorbates and transition states.[119,120] In practice, the local magnetic moment on the active metal is a compact, reportable descriptor of spin polarization. Both the absolute moment and its evolution along the reaction coordinate are informative: they track spin repopulation, spin-channel matching, and barriers to spin flipping/pairing in spin-selective steps.

On $Fe–N_4$ architectures, compressing the inter-site distance into the sub-nanometer regime enhances cooperative effects, tunes local moments and inter-site exchange, and thereby modulates *OOH formation and O–O scission kinetics; experiments on Fe–N–C delineate a distance window for boosted ORR, while theory traces how spin alignment perturbs σ(Fe–O) bonding and redirects the preferred pathway.[17] Heteronuclear pairs add an extra degree of freedom: cross-site charge transfer typically induces spin repolarization and a functional division of labor accompanied by redistribution of magnetic moments. For Fe–Co diatomics, *operando* spectroscopy and DFT support a Janus-like behavior where Co favors the $4e^-$ ORR route while Fe stabilizes *OH; computed site-resolved magnetic moments vary along the sequence, consistent with Co-centered *OOH handling as the rate-relevant step.[121] Independent studies further show that broken-symmetry Fe–Co pairs with asymmetric spin states exhibit enhanced ORR/OER kinetics.[122] In a complementary yet mechanistically milder scenario, Fe–Ni pairs do not rely on pronounced spin repolarization; instead, moderate spin polarization together with Fe-3d delocalization correlates with improved bifunctional activity.[123]

Spin state can also be ligand-field-programmed by a neighboring heterometal: in Fe–Mn/N–C, adjacent Mn–N moieties stabilize intermediate-spin Fe(III) ($t_{2g}^4e\_g^1$) at $Fe–N_4$ and elevate acidic-ORR activity.[124] Even in Ru-containing systems, where charge/polarization effects dominate and direct Ru–Ru bonding is weak, spin features remain tunable. Adjusting inter-metal distances or compositions within Fe–Co–Ni–Ru multi-SACs landscapes reshapes the DOS and predicted metrics; external fields can also trigger spin transitions on Ru–

N–C single-atom motifs, enabling "lightweight spin engineering" on nominally nonmagnetic carbons.[125]

3.2 Synergistic adsorption and activation

3.2.1 Terminal *vs.* bridging occupancy and its implications. In DACs, terminal adsorption (θ_terminal, binding to one metal center) and bridging adsorption (θ_bridging, binding across two centers) differ not only in geometry but also in site occupancy and fractional coverage under operating conditions. The relative population of these two states is not fixed and can vary with applied potential, electrolyte identity, surface coverage, and intermetal distance. As a result, DACs surfaces may exhibit different working-state fractions during reaction. Recent mechanistic studies further demonstrate that varying d_{M-M} modifies the electrochemically induced surface coverage of M–N–C dual-atom catalysts, thereby shifting the preferred adsorption mode under working potentials.[26,102]

This distribution between terminal and bridging adsorption has important kinetic and selectivity implications. First, bridging adsorption occupies two adjacent metal centers per adsorbate, effectively reducing the number of independently available active sites. Consequently, reporting apparent turnover frequencies per metal atom or per metal pair may lead to different interpretations. Second, bridging configurations enable genuine two-center transition states and reaction pathways that cannot arise from purely terminal binding. In contrast, when terminal adsorption dominates, more individual sites remain accessible, but the reaction may proceed through single-site-like mechanisms with different rate-determining steps and product distributions.

3.2.2 Bridging occupancy and the distance-matching rule. When θ_bridging becomes significant, a useful geometric guideline is the distance-matching rule. In DACs, d_{M-M} matching is a general geometric guideline: when the d_{M-M} matches the surface-projected span and orientation of the substrate or the key transition state, the molecule anchors to both metals simultaneously and forms a stable bidentate/bridged geometry. Critically, the RDS proceeds *via* a *bona fide* two-center transition state with both metals concurrently participating.

Compared with single-site binding (θ_terminal), this dual-site mode (θ_bridging) confers two practical advantages. First, kinetic facilitation with an expanded operating window: dual anchoring preorganizes the transition state, cutting conformational search and entropic cost from adsorption to activation, while two moderate contacts avoid the "too-tight" binding typical of a single site; as a result, apparent barriers drop and high turnover can be maintained across a broader potential/temperature range. This behavior is repeatedly observed in ORR, where adjacent $Fe-N_4-Fe-N_4$ or Pt–Pt sites display activity peaks within a sub-nanometer to near-nanometer window consistent with dual-site O_2/*OOH anchoring and O–O elongation; array-based distance tuning on carbon supports yields a clear volcano trend.[17,40,95] For COOH nucleation on Ni–Cu pairs, the rate-determining transition state is two-center: the nascent carboxyl headgroup adopts a bridged/bidentate geometry in which Ni and Cu concurrently coordinate/polarize distinct lobes (C- and O-ends) of the intermediate, yielding a single saddle point that does not exist on single-site models and a lower Gibbs free energy of activation than either $Ni-N_4$ or $Cu-N_4$.[49,62] Likewise, Fe–Fe and Fe–Ni pairs at commensurate spacings stabilize bridged *COOH *via* a two-center transition state.[29,46,51] However, the mere presence of adjacent metal centers does not guarantee efficient dual-site coupling. For example, detailed analyses of CO_2 reduction on DACs reveal that C–C coupling remains kinetically challenging when adsorption energetics and surface coverage are not optimally tuned, even on dual-atom configurations.[30]

Second, pathway steering and selectivity enhancement: a well-posed bridged geometry biases the reaction toward the desired channel and suppresses side routes. On Mo_2C-supported quasi-paired Pt, only specific Pt–Pt separations stabilize bridged *OOH and promote clean O–O scission, preserving durable $4e^-$ ORR instead of the $2e^-$ peroxide path.[40,95] A tunable Ru–Ru system offers mechanism-level proof: at about 6.2 Å average spacing, uric acid undergoes *bona fide* dual-site co-adsorption and the electro-oxidation switches from a conventional two-electron route to a three-electron pathway, with concomitant gains in sensitivity and intrinsic activity; expanding the spacing to 7.0–9.3 Å reverts adsorption to a single site and restores the two-electron route.[102] In thermocatalytic hydrodehalogenation, neighboring Pd single atoms outperform isolated atoms and nanoparticles only at separations that permit a genuine two-center geometry, where one site cleaves the C–X bond while the partner directionally stabilizes the leaving group.[31]

The geometric design principles discussed above implicitly assume that diatomic motifs remain structurally intact under reaction conditions. However, recent *operando* XAFS studies reveal that this assumption does not universally hold. In heteronuclear Cu–Ni systems,[126] asymmetric atomic pairs undergo potential-dependent in-plane reconstruction during CO_2 electroreduction, progressively evolving into Cu-rich Cu_x–Ni atomic clusters ($x = 3–7$), accompanied by Cu valence reduction and increased Cu–Cu coordination numbers. Such findings demonstrate that d_{M-M} is not necessarily a static descriptor but may itself be a potential-dependent variable. Consequently, distance-matching rules and dual-site transition-state models must be interpreted within the stability window of the diatomic motif under working conditions.

Taken together, these examples show that the d_{M-M} is a key structural parameter in DACs design. By tuning this distance to match the size and geometry of the relevant transition state, the catalyst can better stabilize reactive intermediates and guide the reaction along a desired pathway. In practice, deliberately engineering the appropriate intersite spacing provides a concrete strategy to improve activity, enhance selectivity, and maintain structural stability under operating conditions.

3.3 Tandem effects

Tandem effects in DACs emphasize temporal partitioning and in-place handoff: two adjacent atoms are each optimal for different steps in the sequence, enabling sub-nanometer neighboring-site transfer or spillover of intermediates. This short-range relay circumvents the intrinsic single-site trade-off between activation and release. The canonical case is CO_2-to-CO electroreduction on Fe–Ni pairs:[46] Fe forms *COOH at low overpotential, a fast start, whereas adjacent Ni binds *CO more weakly and promotes desorption, a clean finish. Their proximity enables *in situ* transfer of the carboxyl intermediate to an adsorbed CO intermediate without long-range diffusion, leading to higher CO partial current density and higher CO faradaic efficiency over a broad potential window; by contrast, physical mixtures or widely separated Fe + Ni fail to reproduce this current–selectivity synergy.[127,128] Ni–Cu pairs show the same logic: Ni accelerates *COOH nucleation, while neighboring Cu facilitates *CO release and concurrently suppresses HER, preserving CO selectivity even at high current densities.[62] A similar early activation and late release division extends to Fe–Cu and Fe–Co combinations.[121,129] In thermocatalytic hydrodehalogenation, adjacent Pd single atoms realize a relay from C–X cleavage at one site to halide capture/transfer at the other, outperforming both isolated atoms and nanoparticles in turnover and selectivity.[31] In aerobic ammoxidation under ambient conditions, low-coordinated Co–Ru dual atoms enact temporal partitioning with in-place handoff:[130] CoN_3 activates O_2 to $O_2^{-\bullet}$/OOH*, then the oxidizing equivalent relays over Å-scale proximity to RuN_3 that binds the imine. This genuine tandem relay slashes the N–H/C–H barriers, outperforming single-atom controls and post-loaded mixtures.

A closely related, photochemical manifestation of this tandem principle appears in vacancy-rich MOFs bearing Cu–Ti dual-metal pairs:[131] The Ti node acts as the primary photoabsorber and CO_2-activation center, while the neighboring Cu single atom directs the downstream hydrogenation and the C–C coupling from *CHO to *CHOCO. Ultrafast charge transfer from Ti to Cu (~3 ps), together with light-induced structural self-regulation, turns an otherwise unfavorable coupling into a spontaneous, high-selectivity pathway to C_2 products. Likewise in photocatalytic nitrate-to-ammonia conversion, Ag–Cu dual single atoms on g-C_3N_4 embody a spatially decoupled tandem relay:[132] Cu_1 binds and activates NO_3^-, the NO and NOH intermediates migrate to a nearby Ag_1 site that is inert to hydrogen evolution yet effective for deep hydrogenation, yielding 98% NH_3 selectivity at 630.5 μmol g^{-1} h^{-1}; single-atom analogues and physical mixtures do not reproduce this, and DFT identifies an optimal Ag–Cu spacing tested at 3.03, 7.19 and 12.09 Å with a minimum barrier near 0.122 eV and a 1 : 1 Ag : Cu ratio. In line with this, Ni–Zn dual atoms anchored on polymeric carbon nitride rely on sub-nanometer proximity to partition roles:[133] electrons at Zn drive the two-electron ORR *via* *OOH to H_2O_2, while holes at Ni promote the two-electron Water Oxidation Reaction (WOR) *via* *OH. Working within one near-neighbor domain, these paired half-reactions raise H_2O_2 productivity and stability over separated single-atom controls.

Overall, tandem effects furnish diatomic catalysts with a third design pathway distinct from single-site optimization: instead of forcing a single center to perform all tasks along the reaction coordinate, sub-nanometer proximity and functional partitioning allocate different reaction stages to neighboring metal atoms. By encoding appropriate d_{M-M} and site topology in the geometry, introducing cross-site cooperativity at the electronic-structure level, and ensuring a smooth local relay of intermediates in the kinetics, tandem diatomic motifs achieve a more balanced compromise between activation and release, and between activity and selectivity.

4. Machine learning for DACs

Machine learning (ML) is increasingly adopted in DACs research to address two persistent challenges: DACs synthesis spans a coupled and high-dimensional parameter space that includes metal identity, intersite distance, local symmetry, and support coordination. This complexity makes it difficult to disentangle individual variables or establish predictive structure–synthesis relationships.[134,135] and characterization still struggles to jointly capture geometry, electronic structure, and the true working-state population of DACs motifs.[19,28,136] Against this backdrop, ML contributes in two tightly connected ways.

First, atomic-scale metrology from microscopy needs to be objective, scalable, and reproducible. In practice, HAADF-STEM images are frequently noisy and drift-affected, with limited fields of view, which makes manual adjacency identification slow, subjective, and difficult to compare across samples and studies.[137] Recent advances in deep-learning-assisted microscopy analysis enable automated denoising and atom localization at atomic resolution,[138,139] thereby reducing operator bias and improving reproducibility. ML-based workflows can further standardize this process by constructing atomic neighbor graphs to extract comparable structural descriptors—such as single-atom density (ρ_1), candidate pair density (ρ_2), the d_{M-M} distribution, orientation statistics, and pair purity—using graph-based structural representations.[140,141] This transformation converts images from illustrative snapshots into quantitative evidence that can be aggregated and contrasted across batches and operating conditions.

Second, DACs design and selection are inherently combinatorial, spanning metal pairing, coordination environment, support chemistry, inter-site spacing, spin/charge state, coverage, and operating window.[134] Exhaustive DFT or experimental trial-and-error cannot efficiently cover this space.[142] Data-driven surrogate models with chemically interpretable descriptors,[140] coupled with active-learning loops,[143] can prioritize candidates, predict key properties, and propose the next calculations or experiments under quantified uncertainty.[144] Accordingly, this section proceeds in two parts: ML for atomic-scale image-based metrology, followed by ML for DACs screening and design (Table 2).

Table 2 Machine-learning frameworks for DACs image recognition and screening and design

Ref	Task	Algorithm	Inputs	Outputs	Train set	Test set	Accuracy
145	Image recognition	Model-based maximum-likelihood atomic column localization framework (StatSTEM)	HAADF-STEM	Atomic-column positions & intensities (overlap-aware)	—	—	Positioning robust when spacings <2 Å if overlap modeled; no ML split.
146	Image recognition	2D Gaussian fitting–based atomic column metrology framework (Atomap)	HAADF-STEM	Column positions, distances/strain, uncertainties	—	—	Classic metrology workflow; no ML split.
138	Image recognition	Weakly supervised fully convolutional network (FCN) for pixelwise defect segmentation	HAADF-STEM (lattices + multiple defect classes)	Pixelwise class maps → LoG peaks → defect/structure graph; tracking	—	—	Qualitative/benchmarking; split sizes not specified.
147	Image recognition	AtomSegNet (U-Net) on TEMImageNet	HAADF-STEM (Pt, NiO, $SrTiO_3$, $DyScO_3$, Si, graphene, MoS_2, TiO_2; varied conditions)	Atom segmentation/localization; denoise/deblur; Gaussian maps	75% of dataset (ratio reported)	25% of dataset	Final test error ≈0.0195 (MSE-like); Otsu + Gaussian mapping outperforms a Faster R-CNN baseline.
148	Image recognition	Two U-Nets ("localize" + "classify")	Simulated + experimental HAADF-STEM of Pt/CeO_2(≈5 fps)	Sub-pixel positions + particle/support labels; migration tracks	7500 synthetic images	9 manually annotated experimental images (plus synthetic sweeps)	99.43% classification accuracy on manual test.
149	Image recognition	Physics-based iterative STEM parameter optimization framework	HAADF-STEM (low dose; residual non-round aberrations)	Per-atom/column intensities → atom-by-atom chemical identification	—	—	More reliable under noise/aberrations *vs.* established methods.
150	Image restoration	Physics-aware convolutional neural network with adversarial training (RaGAN-based)	TEM/STEM single-shot frames	Restored images (denoise/deblur; contrast/detail)	Trained on six datasets (types described)	—	Restoration quality improved *vs.* L1/L2-only; split sizes not stated.
151	Image recognition	Hybrid rule-based and ML-assisted atomic analysis pipeline	HAADF-STEM	Counts, densities; standardized workflows/resources	—	—	Systematizes automated single-atom analysis; focuses on pipeline/benchmarking.
152	Image recognition	Ensemble deep-learning segmentation model (U-Net architecture)	STM frames	Defect segmentation → coordinates, counts, densities	38 parent images ×60 crops → 2280 patches (STM WSe_2)	100 unseen STM images (+cross-modality tests)	mean average precision ≈ 0.78; harmonic mean of precision and recall ≈ 0.66; area under the receiver operating characteristic curve ≈ 0.97
153	Screening/design (ORR)	Descriptor-based high-throughput DFT screening (volcano analysis; no ML model)	DFT on PtM@C_6N_6	ΔG*OH-centric volcano; near-apex pairs	—	—	Optimum near ~0.98 eV; PtIr@C_6N_6 closest to peak.
154	Screening/design (ORR + OER)	Descriptor engineering + high-throughput DFT ranking framework (*no explicit ML model*) Throughput-DFT volcano	SACs motifs to DACs on N-graphene; 30 × 30 metal pairs; 15 defect configs; DFT ΔG(*O,*OH,*OOH) with computational hydrogen electrode + VASPsol	Unified descriptor φ; predicted ΔG*O/ΔG*OH/ΔG*OOH; volcano-based ORR/OER screening; 17 bifunctional candidates	Combined SACs + DACs dataset	—	The coefficient of determination (R^2): 0.90 (*O), 0.81 (*OH), 0.78 (*OOH)
155	Screening/design (multi-rxn)	Physics-guided sparse regression surrogate model (ARSC framework)	DFT-labeled features for ORR/OER/CO_2RR/nitrogen reduction reaction (NRR)	Predicted activities/overpotentials	—	—	Interpretable surrogates; split not specified.
156	Screening/design (ORR to device)	Active learning on two descriptors (d_{M-M}, magnetic moment)	Candidate DACs on N–C; seed DFT ORR energies; descriptors: d_{M-M} & magnetic moment.	Design map; Co–N–Mn realized; device validated	—	—	Half-wave potential ≈ 0.90 V; peak power density of the zinc–air battery ≈ 271 mW cm^{-2}.

Table 2 *(Contd.)*

Ref	Task	Algorithm	Inputs	Outputs	Train set	Test set	Accuracy
157	Screening/design (cross-supports)	High-throughput DFT screening across support variations (*no ML model*)	DFT across pairs	ORR/OER trends *vs.* zinc–air battery performance	—	—	Emphasis on HT-DFT + performance linkage; no ML split.
158	Screening/design (thermal, γ-Al_2O_3(100))	Supervised ML on DFT-labeled descriptors	γ-Al_2O_3(100)-supported DACs; 435 DFT entries with geometric/electronic features	Predicted PDH activity; CuFe, CuCo, CoZn shortlisted and validated by kinetics	—	—	Model performance discussed qualitatively; split not specified.
159	Screening/design (CO_2 to HCOOH)	Feed-forward NN surrogate	406 DFT-labeled M_1M_2@N-graphene	Predicted limiting potentials; Co–Co–NG & Ir–Fe–NG identified; 64% screening-time reduction *vs.* DFT-only	—	—	Test R^2 = 0.960, root mean square error = 0.319 eV; DFT verification mean absolute error ≈0.14 eV
160	Screening/design (CO_2RR)	Iterative active-learning loop coupling ML surrogate and DFT calculations	Candidate DACs for CO_2RR; seed DFT adsorption energies for key inter-mediates; basic descriptors: d_{M-M}/charge/spin	~70% hit-rate for formate selectivity (≈3 rounds)	—	—	29/42 hits (~70%); 5 unexplored DACs predicted better than Bi.
161	Screening/design (HER)	Graph convolutional neural network (CGCNN) surrogate with DFT validation	435 DACs on N_6-graphene	Predicted HER activity; AuCo@N_6Gr & NiNi@N_6Gr highlighted and DFT-rationalized	—	—	Dataset size and top pairs as reported
162	Screening/design (NRR)	Descriptor-based DFT screening framework (*no ML model*)	Biphenylene-supported DACs; 28 homonuclear dimers (3d/4d/5d)	Limiting potentials/selectivity; low-overpotential candidates identified	—	—	Theoretical predictions only; no ML split.

4.1 Machine learning for atomic-scale image recognition (SACs/DACs)

In SACs and DACs research, identifying atomic coordinates does not by itself confirm true pairing. Distinguishing correlated dual-atom motifs from incidental proximity requires quantitative adjacency metrics and temporal validation. ML formalizes this decision process through neighbor-graph analysis and pair classification, generating reproducible descriptors (ρ_1, ρ_2, d_{M-M} distributions, orientation statistics) together with uncertainty estimates. This structured approach enables reliable comparison across synthesis strategies and strengthens structure–activity interpretation.

First, geometry- and statistics-driven models established the metrological baseline for seeing atoms and pinning them down. De Backer and co-workers[145] developed StatSTEM, a model-based least-squares framework that simultaneously estimates atomic-column positions and intensities across whole HAADF-STEM frames while explicitly accounting for overlap between neighboring columns, thereby retaining high precision even at low dose. The framework was released as an open-source software package under the same name. They further showed that when inter-column spacings drop below ~2 Å, neglecting overlap leads to substantial errors, whereas Gaussian-volume treatments remain robust over the full range, directly impacting the reliability of any downstream pair quantification. Complementing this, Nord *et al.*[146] introduced Atomap, which automates 2D-Gaussian fitting for atomic-column localization and delivers an integrated workflow, from initialization and refinement through distance measurement and shape analysis to uncertainty evaluation, thereby standardizing strain and structural-distortion quantification.

Building on that foundation, deep learning shifted recognition, classification and counting from rule-based engineering to data-driven inference. Ziatdinov and colleagues[138] proposed a weakly supervised FCN that identifies lattice atoms and multiple defect classes, converts softmax maps *via* Laplacian of Gaussian peak picking and NetworkX graph construction into structure–defect graphs, and thus enables chemical/species identification and time-sequence tracking of dopants/defects, scaling up the human-like reading of atomically resolved STEM. They also laid out network architecture and training details such as encoder–decoder heads, augmentation, and noise/blur perturbations that have since become a reusable template. Lin, Xin and co-workers[147] then built TEMImageNet and released AtomSegNet, delivering an end-to-end U-Net–style pipeline for precise atom segmentation/localization together with denoising and deblurring, making batch, cross-material atom-level annotation and inference practical. For fast/low-dose scenarios, Eliasson & Erni[148] assembled a two-U-Net "localize + classify" pipeline that achieves sub-pixel localization and species labeling of Pt/CeO_2 interfacial columns in 5-fps *in situ* series, revealing sub-second, site-specific migration pathways and underscoring ML's necessity for noise-dominated, fast-scan STEM. From a complementary angle, Hofer and co-authors[149] maximized correlation between experiment and simulation using fast convolutional approximations and multi-parameter optimization, jointly tuning aberrations, source size, and atomic scattering, and then used intensity clustering for chemical discrimination, highlighting the power of model–data co-optimization for species assignment.

Because image quality caps recognition performance, single-shot restoration has become a first-class module. Lobato and colleagues[150] combined CNNs with physics-aware losses such as relativistic average GAN terms together with pixel-wise L1/L2 and multi-local whitening transforms to markedly improve contrast and detail in single-exposure EM images, clearing a key obstacle to reliable low-dose localization and chemistry.

Transferring these capabilities to catalytic SAC/DACs systems, the field is converging on automated image-to-metrics workflows. Mitchell *et al.*[151] deployed automated analysis for single-atom detection and counting in catalytic materials, systematizing data-driven TEM needs and explicitly linking to resources such as TEMImageNet/AtomSegNet and unsupervised defect detection—signposting a trajectory toward automation, scale, and traceability. In a broader 2D-materials setting, Smalley *et al.*[152] used an ensemble of U-Net models to extract coordinates, counts, densities, and spatial descriptors for atomic-scale defects in 2H-WSe_2, amassing about 1.6×10^4 detections; the work showcases machine learning's efficiency and reproducibility for low-density defects, large-area statistics, and rapid quality control, exactly the style of metrology SACs/DACs studies require for pair distributions and proximity metrics.

Together, model-based fitting (StatSTEM, Atomap), deep pipelines (weak-supervision, TEMImageNet/AtomSegNet, two-U-Net fast scans), and single-shot restoration now form an auditable image-to-pair workflow that converts atomically resolved EM into DACs-relevant metrics (ρ_1, ρ_2, d_{M-M} distribution, orientations, dynamics). The main gaps are: (i) domain shift and benchmarking—methods still lean on synthetic data and lack DACs-specific, cross-microscope benchmarks for pair detection/purity and proximity statistics; (ii) chemistry assignment under annular dark-field alone—species labeling remains fragile without physics-aware fitting and multimodal fusion (electron energy-loss spectroscopy/energy-dispersive X-ray spectroscopy) and often breaks for low-Z or mixed thickness; (iii) projection/overlap limits—sub-2 Å columns, tilt, and thickness create 3D ambiguities and occlusions that bias pair counts and (iv) Uncertainty Quantification and reporting standards—few studies propagate calibrated uncertainties to final DACs descriptors or report confidence-bound versions of $\rho_1/\rho_2/d_{M-M}$ distribution; addressing these with shared datasets, physics-aware networks, uncertainty-first metrics, and multimodal co-registration will turn "seeing pairs" into reproducible, comparable evidence across all DACs synthesis routes.

4.2 Machine learning for DACs screening and design

Given the vast DACs design space (metal pairing M^1/M^2, coordination and support, coverage and spin, operating environment), a coherent playbook has crystallized. First, physics-grounded and interpretable descriptors compress the space into a navigable map. As an ORR exemplar within a precious-metal subspace, Jia and Yang[153] built ΔG*OH-centric scaling and a volcano on PtM@C_6N_6, showing an optimum near ~0.98 eV and locating seven near-apex pairs (PtZr, PtRh, PtCd, PtCu, PtIr, PtAg, PtHf); PtIr@C_6N_6 lies closest to the peak with the smallest overpotential. They further enumerated a reusable feature set that mixes thermodynamic terms, Bader charge on Pt, electronegativity, and key bond lengths d(Pt–M), d(Pt–O_1/O_2), d(M–O_1/O_2), and d(O–OH). These descriptors are ready-made inputs for supervised surrogates and can seed acquisition functions in active-learning loops. Complementing this descriptor-first view, Li *et al.*[154] proposed an 'active center inheritance' strategy that ports high-performing SACs motifs (M–N_x) into atomically dispersed bimetallic sites, screened 13 500 DACs geometries, identified 17 bifunctional OER/ORR candidates, and distilled a four-feature unified descriptor φ that reliably correlates ΔGOH/ΔGO/ΔGOOH, thereby shrinking the search while preserving interpretability.

Second, surrogate models trained on DFT labels deliver high-throughput predictions. Lin *et al.*[155] introduced the interpretable ARSC framework (Atomic, Reactant, Synergy, and Coordination) with physics-guided feature engineering and sparsification, disentangling how Atomic, Reactant, Synergy, and Coordination factors shape the d-band to cover ORR/OER/CO_2RR/NRR while reducing brute-force DFT demand.

Third, when labels are sparse or expensive, active learning steers new calculations to the most informative points. Liu *et al.*[156] converted compression into an actionable design chart by mapping ORR onto a two-descriptor landscape (d_{M-M} and site magnetic moment), then realized a Co–N–Mn site and validated device metrics. Tamtaji *et al.*[157] extended this idea across supports by screening $M_1M_2N_6$ on N-graphene and tying predictions to zinc-air performance. On the thermal side, Wang *et al.*[158] trained gradient-boosting regressors over geometric/electronic descriptors for >400 DACs on γ-Al_2O_3(100), scaled to about 300 more, and converged on CuFe, CuCo, and CoZn before full kinetic checks.

Finally, when geometries are intricate and strongly coupled, graph neural networks enable end-to-end structure-to-property learning. For CO_2 to HCOOH, Wu *et al.*[159] coupled DFT with a feed-forward network over 406 M_1M_2@N-graphene candidates to cut screening time by roughly two-thirds and elevate Co–Co and Ir–Fe. Ding *et al.*[160] wrapped CO_2RR discovery in an active-learning loop that reached about 70% hits for formate selectivity within three rounds. At the GNN frontier, Boonpalit *et al.*[161] prescreened 435 HER structures on N_6-graphene and closed the loop with DFT rationalization of cooperative H-binding; Pandiyan and Chen[162] ported a similar workflow to NRR on biphenylene.

Overall, these studies sketch early prototypes of how machine learning can assist DACs design rather than a fully established workflow. Physics-guided descriptors compress the design space, surrogate models and active learning pick out promising metal pairs and environments, and graph-based models handle the more complex geometries. In this role, ML does not replace DFT or experiments, but helps focus them on the most informative candidates and extract simple, transferable design rules from the resulting data. At present, however, most demonstrations remain at the level of DFT-labeled datasets and supervised or active-learning surrogates with task-specific, relatively small training sets; genuinely closed-loop "screen–synthesize–test–redesign" pipelines are still limited to proof-of-concept studies.

5. Conclusions and perspectives

DACs are not defined by which metals they contain, but by how far apart those atoms are and how the surrounding coordination field shapes their communication. Seen through this lens, distance-programmed adjacency turns "two atoms" from a curiosity into a tunable variable that couples geometry to electronic behavior across scales. On the build side, the trajectory has shifted from probability to programmability: site-density engineering bias encounters; ordered coordination networks pre-write Å-level spacing and preserve it through conversion; and multinuclear molecular blueprints deliver deterministic d_{M-M} and ligand fields into solids. On the effect side, three levers act in concert: cross-site charge leveling and local polarization rebalance binding, orbital coupling and d–p hybridization reorganize the DOS, and exchange interactions tune spin textures; at intermediate separations these ingredients unlock bridged adsorption and true tandem relays that isolated sites cannot support. Finally, turning proximity into practice demands auditable metrics and integrable engineering. Quantitative pair descriptors align structure claims with evidence; data-efficient, physics-guided models connect these descriptors to activity, selectivity, and durability; and coupling to scalable micro/nanofabrication translates atomically precise motifs into reproducible device platforms. Taken together, DACs shift heterogeneous catalysis toward geometry–electronic co-engineering: adjacency is written, measured, and utilized, allowing catalytic function to be programmed with the same intent currently applied to composition and support chemistry.

Looking ahead, several directions deserve focused attention from a quantify–design–integrate roadmap: (1) Quantitative pair distributions and a data-driven loop: On top of HAADF-STEM two-dimensional projections, adopt multi-tilt stereometry and three-dimensional reconstruction and formalize a pipeline comprising image restoration, atomic localization and identification, adjacency-graph construction, and pair annotation; report ρ_1 and ρ_2, the d_{M-M} distribution, and orientation distributions together with confidence intervals and full uncertainty propagation for coordinates, classes, and pairing decisions so that adjacency becomes auditable three-dimensional metrology. (2) Charge–spin–local-field coupled design: establish a coupled charge, spin, and local field design framework that moves beyond d band tuning by coordinating second shell or axial ligation, heteronuclear coupling, and external electric, magnetic, or strain fields; quantify and model the causal links between spin repolarization, exchange coupling, and multielectron selectivity, and feed the outcomes back into ligand field choices, elemental pairings, and operating conditions. (3) AI-driven and dynamic ensemble design for DACs: future ML frameworks for DACs should extend beyond static descriptors to incorporate time-dependent site occupation and stability under electrochemical bias. Constant-potential *ab initio molecular dynamics* and electrochemical interface modeling have demonstrated the feasibility of describing potential-dependent surface states and adsorbate distributions,[163,164] while microkinetic and kinetic Monte Carlo approaches provide established tools for resolving population-weighted catalytic rates and dynamic site occupation.[165,166] However, current ML-driven catalyst screening remains largely centered on equilibrium descriptors and static structural representations, and systematic integration of dynamic ensemble simulations with surrogate ML models remains limited in DACs systems. Coupling time-dependent simulations with uncertainty-aware ML frameworks could therefore enable prediction of operational stability windows and catalytic response beyond equilibrium assumptions. (4) Deterministic synthesis of heteronuclear DACs: Achieving M^1/M^2 sites with preset metal identity and spacing is still difficult and costly, and many systems revert to statistical distributions. New, milder and more selective pairing strategies are needed to make heteronuclear DACs a general, scalable approach. (5) Coupling with integrated-circuit–style micro/nanofabrication: Couple DACs with integrated circuit–style micro and nanofabrication to convert atomically precise construction into a wafer-level, replicable device platform. Program on-chip d_{M-M} and coordination environments with generic patterning and conformal deposition, backed by wafer-level metrology and clear release criteria. This integration enables arrayed architectures and scalable deployment across electrochemical conversion, gas sensing, and microreactor applications.

Overall, DACs research is beginning to move beyond a purely discovery-driven stage toward more predictive, engineering-oriented workflows, although this transition is still at an early, proof-of-concept phase. When spatial precision meets electronic intent, and when experiment, computation, and artificial intelligence converge within unified metrics, the long-standing "two-atom problem" will evolve into a general paradigm for constructing multiscale catalytic networks—rational, programmable, and integrable.

Conflicts of interest

There are no conflicts to declare.

Data availability

No new data were generated during this study. All analyzed datasets are publicly available and cited appropriately.

Acknowledgements

This work was supported by the National Key Research and Development Program of China (2024YFA1207900); the National Natural Science Foundation of China (12174050, T2321002); the Natural Science Foundation of Jiangsu Province (BK20231411); the New Cornerstone Science Foundation and the XPLORER Prize; the Postgraduate Research & Practice Innovation Program of Jiangsu Province (KYCX24_0500); the Fundamental Research Funds for the Central Universities; and the China Scholarship Council (202406090138).

References

1 L. Zhang, Y. Ren, W. Liu, A. Wang and T. Zhang, *Natl. Sci. Rev.*, 2018, **5**, 653–672.
2 R. Lang, X. Du, Y. Huang, X. Jiang, Q. Zhang, Y. Guo, K. Liu, B. Qiao, A. Wang and T. Zhang, *Chem. Rev.*, 2020, **120**, 11986–12043.
3 F. Kraushofer and G. S. Parkinson, *Chem. Rev.*, 2022, **122**, 14911–14939.
4 V. Putignano, A. Rosato, L. Banci and C. Andreini, *Nucleic Acids Res.*, 2018, **46**, D459–D464.
5 M. Bazayeva, C. Andreini and A. Rosato, *Acta Crystallogr., Sect. D: Struct. Biol.*, 2024, **80**, 362–376.
6 H. Ooka, J. Huang and K. S. Exner, *Front. Energy Res.*, 2021, **9**, 654460.
7 J. Greeley, *Annu. Rev. Chem. Biomol. Eng.*, 2016, **7**, 605–635.
8 A. S. Dobrota and I. A. Pasti, *J. Phys. Chem. Lett.*, 2025, **16**, 77–86.
9 Data-derived enzyme statistics. We queried the Research Collaboratory for Structural Bioinformatics Protein Data Bank snapshot dated 24 October 2025 for entries annotated as enzymes and containing at least one metal atom, then counted the metal atoms from the deposited coordinates and labeled an entry "multi-metal" when the count was two or more. Checks with stricter definitions (transition metals only, occupancy at least 0.5, and metals within 3.0 Å of protein or nucleic acid) yielded similar totals.
10 K. Saito, M. Nakagawa and H. Ishikita, *Commun. Chem.*, 2020, **3**, 89.
11 A. C. Rosenzweig, C. A. Frederick, S. J. Lippard and P. Nordlund, *Nature*, 1993, **366**, 537–543.
12 A. Volbeda, M.-H. Charon, C. Piras, E. C. Hatchikian, M. Frey and J. C. Fontecilla-Camps, *Nature*, 1995, **373**, 580–587.
13 W. Lubitz, H. Ogata, O. Rudiger and E. Reijerse, *Chem. Rev.*, 2014, **114**, 4081–4148.
14 Y. Chen, J. Lin, Q. Pan, X. Liu, T. Ma and X. Wang, *Angew. Chem., Int. Ed.*, 2023, **62**, e202306469.
15 C. Fang, J. Zhou, L. Zhang, W. Wan, Y. Ding and X. Sun, *Nat. Commun.*, 2023, **14**, 4449.
16 Y. Li, Y. Li, H. Sun, L. Gao, X. Jin, Y. Li, Z. Lv, L. Xu, W. Liu and X. Sun, *Nano-Micro Lett.*, 2024, **16**, 139.
17 Z. Jin, P. Li, Y. Meng, Z. Fang, D. Xiao and G. Yu, *Nat. Catal.*, 2021, **4**, 615–622.
18 Y. Yan, R. Yu, M. Liu, Z. Qu, J. Yang, S. He, H. Li and J. Zeng, *Nat. Commun.*, 2025, **16**, 334.
19 C.-C. Hou, H.-F. Wang, C. Li and Q. Xu, *Energy Environ. Sci.*, 2020, **13**, 1658–1693.
20 L. Wang, J. Li, S. Ji, Y. Xiong and D. Wang, *Energy Environ. Sci.*, 2024, **17**, 8482–8528.
21 T. He, A. R. P. Santiago, Y. Kong, M. A. Ahsan, R. Luque, A. Du and H. Pan, *Small*, 2022, **18**, e2106091.
22 J. Xiang, P. Wang, P. Li, M. Zhou, G. Yu and Z. Jin, *Angew. Chem., Int. Ed.*, 2025, **64**, e202500644.
23 R. Xu, R. Sun, H.-Q. Xu, G. Xie and J. Ge, *J. Mater. Chem. A*, 2024, **12**, 26316–26349.
24 A. Pedersen, J. Barrio, A. Li, R. Jervis, D. J. L. Brett, M. M. Titirici and I. E. L. Stephens, *Adv. Energy Mater.*, 2021, **12**, 2102715.
25 W. Yang, Z. Jia, B. Zhou, L. Chen, X. Ding, L. Jiao, H. Zheng, Z. Gao, Q. Wang and H. Li, *ACS Catal.*, 2023, **13**, 9695–9705.
26 W. Yang, Z. Jia, L. Chen, B. Zhou, D. Zhang, Y. Han, Z. Gao and H. Li, *Chem. Commun.*, 2023, **59**, 10761–10764.
27 X. Zheng, J. Yang and D. Wang, *EES Catal.*, 2023, **1**, 665–676.
28 H. Lee, *Chem*, 2025, **11**, 102746.
29 Y. Wang, B. J. Park, V. K. Paidi, R. Huang, Y. Lee, K.-J. Noh, K.-S. Lee and J. W. Han, *ACS Energy Lett.*, 2022, **7**, 640–649.
30 W. Yang, Z. Jia, B. Zhou, L. Wei, Z. Gao and H. Li, *Commun. Chem.*, 2023, **6**, 6.
31 C. Chu, D. Huang, S. Gupta, S. Weon, J. Niu, E. Stavitski, C. Muhich and J. H. Kim, *Nat. Commun.*, 2021, **12**, 5179.
32 S. W. Chee, T. Lunkenbein, R. Schlögl and B. Roldán Cuenya, *Chem. Rev.*, 2023, **123**, 13374–13418.
33 M. J. Jung, A. Razazzadeh, H. Khan and S. H. Kwon, *Exploration*, 2025, **5**, e20240010.
34 J. Luo, G. I. N. Waterhouse, L. Peng and Q. Chen, *Ind. Chem. Mater.*, 2023, **1**, 486–500.
35 X. Yang, B. Zhu, Z. Gao, C. Yang, J. Zhou, A. Han and J. Liu, *Adv. Sci.*, 2024, **11**, e2306594.
36 N. Goyal, F. Li and Y.-b. Hu, *J. Mater. Chem. A*, 2024, **12**, 19685–19719.
37 H. Zeng, Y. Guo, T. Li, G. Chen, J. Qiu, B. He and P. Tang, *Chem. Eng. J.*, 2025, **524**, 169094.
38 S. H. Al-Hilfi, X. Jiang, J. Heuer, S. Akula, K. Tammeveski, G. Hu, J. Yang, H. I. Wang, M. Bonn, K. Landfester, K. Mullen and Y. Zhou, *J. Am. Chem. Soc.*, 2024, **146**, 19886–19895.
39 H. Zhang, J. Wang, J. Yao, Q. Yang, X. Zuo, H. Tang, W. Wang, L. Yang and G. Li, *Angew. Chem., Int. Ed.*, 2025, **64**, e202506563.
40 L. Zhang, T. Yang, W. Zang, Z. Kou, Y. Ma, M. Waqar, X. Liu, L. Zheng, S. J. Pennycook, Z. Liu, X. J. Loh, L. Shen and J. Wang, *Adv. Sci.*, 2021, **8**, e2101344.
41 Y. Lou, F. Jiang, W. Zhu, L. Wang, T. Yao, S. Wang, B. Yang, B. Yang, Y. Zhu and X. Liu, *Appl. Catal., B*, 2021, **291**, 120122.

42 H. Shi, Q. Wang, S. Fang, C. Wang, G. Yang, J. Zeng, J. Li, G. Mele and C. Wang, *Langmuir*, 2025, **41**, 15630–15640.
43 Y. Deng, Y. Lin, M. Zhang, R. Dai, Z. Luo, Q. Zhou, M. Xiang, J. Bai and S. Lu, *Energy Adv.*, 2023, **2**, 805–812.
44 H. Yan, Y. Lin, H. Wu, W. Zhang, Z. Sun, H. Cheng, W. Liu, C. Wang, J. Li, X. Huang, T. Yao, J. Yang, S. Wei and J. Lu, *Nat. Commun.*, 2017, **8**, 1070.
45 J. Zhang, Z. Song, X. Yao, Y. Guan, Z. Huo, N. Chen, L. Zhang and X. Sun, *Chem*, 2025, **11**, 102498.
46 M. Qi, M. J. Zachman, Y. Li, Y. Zeng, S. Hwang, J. Liang, M. Lyons, Q. Zhao, Y. Mao, Y. Shao, Z. Feng, Z. Wang, Y. Zhao and G. Wu, *Energy Environ. Sci.*, 2025, **18**, 5643–5656.
47 M. Xiao, H. Zhang, Y. Chen, J. Zhu, L. Gao, Z. Jin, J. Ge, Z. Jiang, S. Chen, C. Liu and W. Xing, *Nano Energy*, 2018, **46**, 396–403.
48 S. Li, A. Guan, C. Yang, C. Peng, X. Lv, Y. Ji, Y. Quan, Q. Wang, L. Zhang and G. Zheng, *ACS Mater. Lett.*, 2021, **3**, 1729–1737.
49 H. Cheng, X. Wu, M. Feng, X. Li, G. Lei, Z. Fan, D. Pan, F. Cui and G. He, *ACS Catal.*, 2021, **11**, 12673–12681.
50 Y. He, X. Yang, Y. Li, L. Liu, S. Guo, C. Shu, F. Liu, Y. Liu, Q. Tan and G. Wu, *ACS Catal.*, 2022, **12**, 1216–1227.
51 W. Ren, X. Tan, W. Yang, C. Jia, S. Xu, K. Wang, S. C. Smith and C. Zhao, *Angew. Chem., Int. Ed.*, 2019, **58**, 6972–6976.
52 Y. Shu, D. Wang, H. Gu, G. Zhu, K. Fan, B. Liu, M. Zhang, J. Wang, L. Liu, J. Zhang, C. Zhang and H. Huang, *Environ. Sci. Technol.*, 2025, **59**, 20109–20123.
53 M. O. Cichocka, Z. Liang, D. Feng, S. Back, S. Siahrostami, X. Wang, L. Samperisi, Y. Sun, H. Xu, N. Hedin, H. Zheng, X. Zou, H. C. Zhou and Z. Huang, *J. Am. Chem. Soc.*, 2020, **142**, 15386–15395.
54 L. Jiao, R. Zhang, G. Wan, W. Yang, X. Wan, H. Zhou, J. Shui, S. H. Yu and H. L. Jiang, *Nat. Commun.*, 2020, **11**, 2831.
55 S. P. Desai, J. Ye, J. Zheng, M. S. Ferrandon, T. E. Webber, A. E. Platero-Prats, J. Duan, P. Garcia-Holley, D. M. Camaioni, K. W. Chapman, M. Delferro, O. K. Farha, J. L. Fulton, L. Gagliardi, J. A. Lercher, R. L. Penn, A. Stein and C. C. Lu, *J. Am. Chem. Soc.*, 2018, **140**, 15309–15318.
56 A. B. Thompson, D. R. Pahls, V. Bernales, L. C. Gallington, C. D. Malonzo, T. Webber, S. J. Tereniak, T. C. Wang, S. P. Desai, Z. Li, I. S. Kim, L. Gagliardi, R. L. Penn, K. W. Chapman, A. Stein, O. K. Farha, J. T. Hupp, A. B. F. Martinson and C. C. Lu, *Chem. Mater.*, 2016, **28**, 6753–6762.
57 J. García Ponce, M. L. Díaz-Ramírez, S. Gorla, C. Navarathna, G. Sanchez-Lecuona, B. Donnadieu, I. A. Ibarra and V. Montiel-Palma, *CrystEngComm*, 2021, **23**, 7479–7484.
58 M. Mon, M. A. Rivero-Crespo, J. Ferrando-Soria, A. Vidal-Moya, M. Boronat, A. Leyva-Perez, A. Corma, J. C. Hernandez-Garrido, M. Lopez-Haro, J. J. Calvino, G. Ragazzon, A. Credi, D. Armentano and E. Pardo, *Angew. Chem., Int. Ed.*, 2018, **57**, 6186–6191.
59 Y. Zheng, N. Martin, M. Boronat, J. Ferrando-Soria, M. Mon, D. Armentano, E. Pardo and A. Leyva-Perez, *Sci. Rep.*, 2023, **13**, 10376.
60 D. Sun and Z. Li, *J. Phys. Chem. C*, 2016, **120**, 19744–19750.
61 Z. Jiang, X. Liu, X. Z. Liu, S. Huang, Y. Liu, Z. C. Yao, Y. Zhang, Q. H. Zhang, L. Gu, L. R. Zheng, L. Li, J. Zhang, Y. Fan, T. Tang, Z. Zhuang and J. S. Hu, *Nat. Commun.*, 2023, **14**, 1822.
62 J. Zhu, M. Xiao, D. Ren, R. Gao, X. Liu, Z. Zhang, D. Luo, W. Xing, D. Su, A. Yu and Z. Chen, *J. Am. Chem. Soc.*, 2022, **144**, 9661–9671.
63 C. Yang, K. Jiang, Q. Zheng, X. Li, H. Mao, W. Zhong, C. Chen, B. Sun, H. Zheng, X. Zhuang, J. A. Reimer, Y. Liu and J. Zhang, *J. Am. Chem. Soc.*, 2021, **143**, 17701–17707.
64 Y. Yue, P. Cai, K. Xu, H. Li, H. Chen, H. C. Zhou and N. Huang, *J. Am. Chem. Soc.*, 2021, **143**, 18052–18060.
65 Z. Zhang, S. Qi, J. Wang and M. Zhao, *Appl. Surf. Sci.*, 2021, **563**, 150352.
66 X. Yang, X. Li, M. Liu, S. Yang, Q. Xu and G. Zeng, *Small*, 2024, **20**, e2306295.
67 X. Chen, C. Liu, T. Yang, X. Jiang, Y. Yang, J. Su, J. Yi and Y. Dong, *Appl. Catal., B*, 2025, **377**, 125499.
68 S. Yang, Y. Wei, X. Li, J. Mao, B. Mei, Q. Xu, X. Li and Z. Jiang, *Angew. Chem., Int. Ed.*, 2023, **62**, e202313029.
69 M. Liu, S. Liu, Q. Xu, Q. Miao, S. Yang, S. Hanson, G. Z. Chen, J. He, Z. Jiang and G. Zeng, *Carbon Energy*, 2023, **5**, e300.
70 Q. Miao, Z. Chen, X. Li, M. Liu, G. Liu, X. Yang, Z. Guo, C. Yu, Q. Xu and G. Zeng, *ACS Catal.*, 2023, **13**, 11127–11135.
71 R. Dun, X. He, J. Huang, W. Wang, l. Yiwei, L. Li, B. Lu, Z. Hua and J. Shi, *J. Mater. Chem. A*, 2023, **11**, 5902–5909.
72 X. He, Q. He, Y. Deng, M. Peng, H. Chen, Y. Zhang, S. Yao, M. Zhang, D. Xiao, D. Ma, B. Ge and H. Ji, *Nat. Commun.*, 2019, **10**, 3663.
73 H. Gu, X. Liu, X. Liu, C. Ling, K. Wei, G. Zhan, Y. Guo and L. Zhang, *Nat. Commun.*, 2021, **12**, 5422.
74 W. Liu, G. Long, Z. Xiang, T. Ren, J. Piao, K. Wan, Z. Fu and Z. Liang, *Angew. Chem., Int. Ed.*, 2024, **63**, e202411014.
75 T. Chen, W. Yu, C. K. T. Wun, T. S. Wu, M. Sun, S. J. Day, Z. Li, B. Yuan, Y. Wang, M. Li, Z. Wang, Y. K. Peng, W. Y. Yu, K. Y. Wong, B. Huang, T. Liang and T. W. B. Lo, *J. Am. Chem. Soc.*, 2023, **145**, 8464–8473.
76 M. Meier, J. Hulva, Z. Jakub, F. Kraushofer, M. Bobić, R. Bliem, M. Setvin, M. Schmid, U. Diebold, C. Franchini and G. S. Parkinson, *Sci. Adv.*, 2022, **8**, eabn4580.
77 C. Wang, P. Sombut, L. Puntscher, Z. Jakub, M. Meier, J. Pavelec, R. Bliem, M. Schmid, U. Diebold, C. Franchini and G. S. Parkinson, *Angew. Chem., Int. Ed.*, 2024, **63**, e202317347.
78 X. Hai, Y. Zheng, Q. Yu, N. Guo, S. Xi, X. Zhao, S. Mitchell, X. Luo, V. Tulus, M. Wang, X. Sheng, L. Ren, X. Long, J. Li, P. He, H. Lin, Y. Cui, X. Peng, J. Shi, J. Wu, C. Zhang, R. Zou, G. Guillen-Gosalbez, J. Perez-Ramirez, M. J. Koh, Y. Zhu, J. Li and J. Lu, *Nature*, 2023, **622**, 754–760.

79 Z. Chen, X. Liao, C. Sun, K. Zhao, D. Ye, J. Li, G. Wu, J. Fang, H. Zhao and J. Zhang, *Appl. Catal., B*, 2021, **288**, 120021.
80 Y. Li, H. Wang, C. Chen, X. Xie, Y. Yang, X. Tan, K. Jiang, N. Chen, H. Zhang and Z. Li, *Nat. Commun.*, 2025, **16**, 8085.
81 H. Zhang, X. Jin, J. M. Lee and X. Wang, *ACS Nano*, 2022, **16**, 17572–17592.
82 W. A. Carole and T. J. Colacot, *Chem. – Eur. J.*, 2016, **22**, 7686–7695.
83 Y. Ma, S. Liu, J. Mao, M. Sun, K. Shi, W. Li, W. Zhao, J. Shan, Y. Zhao, Z. Jiang, R. Zhang, R. Gao, W. Liu, B. Huang, G. Q. M. Lu, J. Liu and L. Wu, *Nat. Mater.*, 2026, **25**, 80–90.
84 D. Yang, P. Xu, E. Guan, N. D. Browning and B. C. Gates, *J. Catal.*, 2016, **338**, 12–20.
85 G. Sun, Y. Cao, D. Li, M. Hu, X. Liang, Z. Wang, Z. Cai, F. Shen, B. Chen and K. Zhou, *Appl. Catal., A*, 2023, **651**, 119025.
86 E. Vorobyeva, E. Fako, Z. Chen, S. M. Collins, D. Johnstone, P. A. Midgley, R. Hauert, O. V. Safonova, G. Vile, N. Lopez, S. Mitchell and J. Perez-Ramirez, *Angew. Chem., Int. Ed.*, 2019, **58**, 8724–8729.
87 Y. S. Wei, L. Sun, M. Wang, J. Hong, L. Zou, H. Liu, Y. Wang, M. Zhang, Z. Liu, Y. Li, S. Horike, K. Suenaga and Q. Xu, *Angew. Chem., Int. Ed.*, 2020, **59**, 16013–16022.
88 T. Tang, X. Xu, X. Bai, C. Hou, T. Gan, Z. Wang and J. Guan, *Angew. Chem., Int. Ed.*, 2025, **64**, e202503019.
89 W. Ye, S. Chen, Y. Lin, L. Yang, S. Chen, X. Zheng, Z. Qi, C. Wang, R. Long, M. Chen, J. Zhu, P. Gao, L. Song, J. Jiang and Y. Xiong, *Chem*, 2019, **5**, 2865–2878.
90 S. Tian, Q. Fu, W. Chen, Q. Feng, Z. Chen, J. Zhang, W. C. Cheong, R. Yu, L. Gu, J. Dong, J. Luo, C. Chen, Q. Peng, C. Draxl, D. Wang and Y. Li, *Nat. Commun.*, 2018, **9**, 2353.
91 N. Wu, H. Zhong, Y. Zhang, X. Wei, L. Jiao, Z. Wu, J. Huang, H. Wang, S. P. Beckman, W. Gu and C. Zhu, *Biosens. Bioelectron.*, 2022, **216**, 114609.
92 Y. Zhao, K. R. Yang, Z. Wang, X. Yan, S. Cao, Y. Ye, Q. Dong and X. Zhang, *Proc. Natl. Acad. Sci. U. S. A.*, 2018, **115**, 2902–2907.
93 T. Ding, X. Liu, Z. Tao, T. Liu, T. Chen, W. Zhang, X. Shen, D. Liu, S. Wang, B. Pang, D. Wu, L. Cao, L. Wang, T. Liu, Y. Li, H. Sheng, M. Zhu and T. Yao, *J. Am. Chem. Soc.*, 2021, **143**, 11317–11324.
94 S. Tian, B. Wang, W. Gong, Z. He, Q. Xu, W. Chen, Q. Zhang, Y. Zhu, J. Yang, Q. Fu, C. Chen, Y. Bu, L. Gu, X. Sun, H. Zhao, D. Wang and Y. Li, *Nat. Commun.*, 2021, **12**, 3181.
95 Y. Xie, X. Chen, K. Sun, J. Zhang, W. H. Lai, H. Liu and G. Wang, *Angew. Chem., Int. Ed.*, 2023, **62**, e202301833.
96 H. Chen, Y. Zhang, Q. He, H. Zhang, S. Xu, X. He and H. Ji, *J. Mater. Chem. A*, 2020, **8**, 2364–2368.
97 N. Zhang, X. Zhang, Y. Kang, C. Ye, R. Jin, H. Yan, R. Lin, J. Yang, Q. Xu, Y. Wang, Q. Zhang, L. Gu, L. Liu, W. Song, J. Liu, D. Wang and Y. Li, *Angew. Chem., Int. Ed.*, 2021, **60**, 13388–13393.
98 J. Sun, T. Tang, S. Zhang, S. Chen, Y. Duan, X. Bai, X. Xu, X. Niu, Z. Wang and J. Guan, *Angew. Chem., Int. Ed.*, 2025, **64**, e202509063.
99 Y. Wang, X. Wan, J. Liu, W. Li, Y. Li, X. Guo, X. Liu, J. Shang and J. Shui, *Nano Res.*, 2021, **15**, 3082–3089.
100 X.-M. Liang, H.-J. Wang, C. Zhang, D.-C. Zhong and T.-B. Lu, *Appl. Catal., B*, 2023, **322**, 122073.
101 B. Jiang, J. Zhu, Z. Xia, J. Lyu, X. Li, L. Zheng, C. Chen, S. Chaemchuen, T. Bu, F. Verpoort, S. Mu, J. Wu, J. Wang and Z. Kou, *Adv. Mater.*, 2024, **36**, e2310699.
102 B. Jiang, H. Zhang, R. Pan, M. Ji, L. Zhu, G. Zhang, J. Liu, H. Shi, H. Huang, S. Wan, K. Yin and L. Sun, *Angew. Chem., Int. Ed.*, 2025, **64**, e202500474.
103 M. Liu, N. Li, S. Cao, X. Wang, X. Lu, L. Kong, Y. Xu and X. H. Bu, *Adv. Mater.*, 2022, **34**, e2107421.
104 D. Fa, J. Yuan, G. Feng, S. Lei and W. Hu, *Angew. Chem., Int. Ed.*, 2023, **62**, e202300532.
105 W. D. Zhang, L. Zhou, Y. X. Shi, Y. Liu, H. Xu, X. Yan, Y. Zhao, Y. Jiang, J. Zhang and Z. G. Gu, *Angew. Chem., Int. Ed.*, 2023, **62**, e202304412.
106 J. Barrio, A. Pedersen, J. Feng, S. C. Sarma, M. Wang, A. Y. Li, H. Yadegari, H. Luo, M. P. Ryan, M. M. Titirici and I. E. L. Stephens, *J. Mater. Chem. A*, 2022, **10**, 6023–6030.
107 Q. Sun, X. Yue, L. Yu, F. Z. Li, Y. Zheng, M. T. Liu, J. Z. Peng, X. Hu, H. M. Chen, L. Li and J. Gu, *J. Am. Chem. Soc.*, 2024, **146**, 35295–35304.
108 Z. Zhang, Z. Xing, X. Luo, C. Cheng and X. Liu, *Nat. Commun.*, 2025, **16**, 921.
109 D. Xue, Y. Zhao, J. Cao, Y. Wang, X. Li and T. Ma, *Adv. Mater.*, 2025, **37**, e2504213.
110 M. Huang, H. Meng, J. Luo, H. Li, Y. Feng and X. X. Xue, *J. Phys. Chem. Lett.*, 2023, **14**, 1674–1683.
111 H. Li, Q. Quan, C. Y. Wong and J. C. Ho, *Adv. Energy Sustainability Res.*, 2025, **6**, 2400326.
112 U. Aschauer and H. Kabbour, *Dalton Trans.*, 2025, **54**, 12118–12124.
113 M. Tsipoaka and A. A. Rownaghi, *Adv. Energy Mater.*, 2025, **15**, 2500635.
114 J. Qin, H. Liu, P. Zou, R. Zhang, C. Wang and H. L. Xin, *J. Am. Chem. Soc.*, 2022, **144**, 2197–2207.
115 J. Qiao, C. Lu, L. Kong, J. Zhang, Q. Lin, H. Huang, C. Li, W. He, M. Zhou and Z. Sun, *Adv. Funct. Mater.*, 2024, **34**, 2409794.
116 X. Yang, D. Xia, Y. Kang, H. Du, F. Kang, L. Gan and J. Li, *Adv. Sci.*, 2020, **7**, 2000176.
117 S. Sarkar, A. Biswas, E. E. Siddharthan, R. Thapa and R. S. Dey, *ACS Nano*, 2022, **16**, 7890–7903.
118 L. Liu, S. Zhang, G. Li, Y. Zhe, J. Liu, X. Zhang, J. Wei, X. Sun, Y. Li and X.-D. Zhang, *Nano Res.*, 2024, **17**, 5872–5883.
119 J. Li, J. Ma, Z. Ma, E. Zhao, K. Du, J. Guo and T. Ling, *Adv. Energy Sustainability Res.*, 2021, **2**, 13374–13418.

120 A. Yu, Y. Zhang, S. Zhu, T. Wu and Z. J. Xu, *Nat. Energy*, 2025, **10**, 435–447.
121 L. J. Yuan, Z. Y. Miao, X. L. Sui, C. F. Lee, Q. Li, M. J. Yin, L. X. Shen, Y. R. Lu, Z. G. Zhao, Y. Z. Liu, L. S. Zhu, W. Gong, W. L. Feng, H. T. Wang, G. X. Zhang and Z. B. Wang, *Nat. Commun.*, 2025, **16**, 7198.
122 X. Li, J. Qin, Q. Lin, X. Yi, C. Yan, J. Zhang, J. Dong, K. Yu, S. Zhang, C. Xie, H. Yang, W. Xiao, W. Li, J. Wang and X. Li, *Adv. Sci.*, 2024, **11**, e2401187.
123 H. Li, J. Wang, R. Qi, Y. Hu, J. Zhang, H. Zhao, J. Zhang and Y. Zhao, *Appl. Catal., B*, 2021, **285**, 119778.
124 G. Yang, J. Zhu, P. Yuan, Y. Hu, G. Qu, B. A. Lu, X. Xue, H. Yin, W. Cheng, J. Cheng, W. Xu, J. Li, J. Hu, S. Mu and J. N. Zhang, *Nat. Commun.*, 2021, **12**, 1734.
125 M. Tamtaji, M. G. Kim, J. Wang, P. R. Galligan, H. Zhu, F. F. Hung, Z. Xu, Y. Zhu, Z. Luo, W. A. Goddard and G. Chen, *Adv. Sci.*, 2024, **11**, e2309883.
126 K. Cheng, D. Shen, Y. Xia, K. Dai, C. Shao, Y. Jiang and Y. Chen, *Angew. Chem., Int. Ed.*, 2025, **64**, e202508932.
127 F. Pan, T. Jin, W. Yang, H. Li, Y. Cao, J. Hu, X. Zhou, H. Liu and X. Duan, *Chem Catal.*, 2021, **1**, 734–745.
128 F.-Z. Li, H.-G. Qin, H.-L. Zhang, X. Yue, L.-K. Fu, B. Xu, M. Lin and J. Gu, *Joule*, 2024, **8**, 1772–1789.
129 H. Yang, H. Huang, Q. Wang, L. Shang, T. Zhang and S. Wang, *J. Mater. Chem. A*, 2023, **11**, 6191–6197.
130 J. Yang, Z. Fang, Z. Sun, W. Zhou, B. Nan, X. Liu, Z. Ma, R. Nie and J. Fu, *Nat. Commun.*, 2025, **16**, 9351.
131 W. Song, B. Song, Y. Liang, Y. Zhou, B. Wang, W. Gao, Y. Wu, X. Ling, Y. Liu, R. Ye, Q. He, T. C. Sum, Y. Yao, Z. Lin, Z. Zou and B. Liu, *J. Am. Chem. Soc.*, 2025, **147**, 39505–39515.
132 Z. Lian, D. Luo, J. Yang, Y. Yang, S. Tang, H. Li, D. Zhang and H. Li, *Angew. Chem., Int. Ed.*, 2026, **65**, e202516964.
133 J. R. Huang, H. Y. Chen, H. L. Zhu, P. Q. Liao and X. M. Chen, *J. Am. Chem. Soc.*, 2025, **147**, 37167–37175.
134 Z. W. Ulissi, M. T. Tang, J. Xiao, X. Liu, D. A. Torelli, M. Karamad, K. Cummins, C. Hahn, N. S. Lewis, T. F. Jaramillo, K. Chan and J. K. Nørskov, *ACS Catal.*, 2017, **7**, 6600–6608.
135 K. Tran and Z. W. Ulissi, *Nat. Catal.*, 2018, **1**, 696–703.
136 J. Wang, C.-X. Zhao, J.-N. Liu, Y.-W. Song, J.-Q. Huang and B.-Q. Li, *Nano Energy*, 2022, **104**, 107927.
137 C. Ophus, *Microsc. Microanal.*, 2019, **25**, 563–582.
138 M. Ziatdinov, O. Dyck, A. Maksov, X. Li, X. Sang, K. Xiao, R. R. Unocic, R. Vasudevan, S. Jesse and S. V. Kalinin, *ACS Nano*, 2017, **11**, 12742–12752.
139 K. Ma, S. Feng, H. Hu, Y. Cai, D. Chen and L. Han, *Chin. J. Struct. Chem.*, 2025, **44**, 100572.
140 T. Xie and J. C. Grossman, *Phys. Rev. Lett.*, 2018, **120**, 145301.
141 C. Chen, W. Ye, Y. Zuo, C. Zheng and S. P. Ong, *Chem. Mater.*, 2019, **31**, 3564–3572.
142 K. T. Butler, D. W. Davies, H. Cartwright, O. Isayev and A. Walsh, *Nature*, 2018, **559**, 547–555.
143 M. Zhong, K. Tran, Y. Min, C. Wang, Z. Wang, C. T. Dinh, P. De Luna, Z. Yu, A. S. Rasouli, P. Brodersen, S. Sun, O. Voznyy, C. S. Tan, M. Askerka, F. Che, M. Liu, A. Seifitokaldani, Y. Pang, S. C. Lo, A. Ip, Z. Ulissi and E. H. Sargent, *Nature*, 2020, **581**, 178–183.
144 J. P. Janet, C. Duan, T. Yang, A. Nandy and H. J. Kulik, *Chem. Sci.*, 2019, **10**, 7913–7922.
145 A. De Backer, K. H. W. van den Bos, W. Van den Broek, J. Sijbers and S. Van Aert, *Ultramicroscopy*, 2016, **171**, 104–116.
146 M. Nord, P. E. Vullum, I. MacLaren, T. Tybell and R. Holmestad, *Adv. Struct. Chem. Imaging*, 2017, **3**, 9.
147 R. Lin, R. Zhang, C. Wang, X. Q. Yang and H. L. Xin, *Sci. Rep.*, 2021, **11**, 5386.
148 H. Eliasson and R. Erni, *npj Comput. Mater.*, 2024, **10**, 168.
149 C. Hofer, V. Skakalova, J. Haas, X. Wang, K. Braun, R. S. Pennington and J. C. Meyer, *Ultramicroscopy*, 2021, **227**, 113292.
150 I. Lobato, T. Friedrich and S. Van Aert, *npj Comput. Mater.*, 2024, **10**, 10.
151 S. Mitchell, F. Pares, D. F. Akl, S. M. Collins, D. M. Kepaptsoglou, Q. M. Ramasse, D. Garcia-Gasulla, J. Perez-Ramirez and N. Lopez, *J. Am. Chem. Soc.*, 2022, **144**, 8018–8029.
152 D. Smalley, S. D. Lough, L. N. Holtzman, M. Holbrook, J. C. Hone, K. Barmak and M. Ishigami, *APL Mach. Learn.*, 2024, **2**, 036104.
153 J. Jia and L. M. Yang, *Adv. Energy Mater.*, 2025, **15**, e03969.
154 W. Li, Y. Mo, L. Kang, C. Li, J. Zheng and C. Qiu, *ACS Catal.*, 2025, **15**, 17689–17702.
155 X. Lin, X. Du, S. Wu, S. Zhen, W. Liu, C. Pei, P. Zhang, Z. J. Zhao and J. Gong, *Nat. Commun.*, 2024, **15**, 8169.
156 Y. Liu, Y. Yang, X. Lin, Y. Lin, Z. Zhuo, D. Liu, J. Mao and J. Jiang, *Nat. Commun.*, 2025, **16**, 5158.
157 M. Tamtaji, M. G. Kim, Z. Li, S. Cai, J. Wang, P. R. Galligan, F.-F. Hung, H. Guo, S. Chen, Z. Luo, W. Wu, W. A. Goddard III and G. Chen, *Nano Energy*, 2024, **126**, 109634.
158 X. Wang, Y. Ma, Y. Li, L. Wang and L. Chi, *Phys. Chem. Chem. Phys.*, 2024, **26**, 22286–22291.
159 H. Zhu, Z. Guo, D. Lan, S. Liu, M. Liu, J. Zhang, X. Luo, J. Yu and T. Wu, *J. Energy Chem.*, 2024, **99**, 627–635.
160 H. Ding, Y. Shi, Z. Li, S. Wang, Y. Liang, H. Feng, Y. Deng, X. Song, P. Pu and X. Zhang, *ACS Appl. Mater. Interfaces*, 2023, **15**, 12986–12997.
161 K. Boonpalit, Y. Wongnongwa, C. Prommin, S. Nutanong and S. Namuangruk, *ACS Appl. Energy Mater.*, 2023, **15**, 12936–12945.
162 K. Pandiyan, D. K. D. Chittibabu and H.-T. Chen, *ACS Appl. Energy Mater.*, 2024, **7**, 10758–10769.
163 N. Bonnet, T. Morishita, O. Sugino and M. Otani, *Phys. Rev. Lett.*, 2012, **109**, 266101.
164 K. Chan and J. K. Norskov, *J. Phys. Chem. Lett.*, 2015, **6**, 2663–2668.
165 A. J. Medford, A. Vojvodic, J. S. Hummelshøj, J. Voss, F. Abild-Pedersen, F. Studt, T. Bligaard, A. Nilsson and J. K. Nørskov, *J. Catal.*, 2015, **328**, 36–42.
166 M. Stamatakis and D. G. Vlachos, *J. Chem. Phys.*, 2011, **134**, 214115.